Journal of Inorganic Biochemistry 275 (2026) 113130

Contents lists available at ScienceDirect

Journal of Inorganic Biochemistry

journal homepage: www.elsevier.com/locate/jinorgbio

Targeting monocarboxylate transporter 1 with a copper-chelating coumarin-based bioconjugate: Synthesis and characterization☆

Matteo Mari [a], Silvia Belluti [b], Luca Pampanella [b], Carol Imbriano [b], Alfonso Zambon [a], Jennifer Storchi [a], Laura Pigani [a], Marianna Tosato [c], Sara Rubagotti [c], Pier Cesare Capponi [c], Mattia Asti [c], Véronique Patinec [d], Raphaël Tripier [d,*], Erika Ferrari [a,*]

[a] Department of Chemical and Geological Sciences, University of Modena and Reggio Emilia, 41125 Modena, Italy
[b] Department of Life Sciences, University of Modena and Reggio Emilia, 41125 Modena, Italy
[c] Radiopharmaceutical Chemistry Laboratory, Nuclear Medicine Unit, AUSL-IRCCS Reggio Emilia, 42122 Reggio Emilia, Italy
[d] Univ Brest, UMR CNRS 6521 CEMCA, 6 avenue Victor Le Gorgeu, F29200 Brest, France

ARTICLE INFO

Keywords:
Monocarboxylate transporters
Coumarin
TACN-based chelators
Copper
Prostate cancer

ABSTRACT

Monocarboxylate Transporters (MCTs), particularly MCT1, are increasingly recognized as key regulators of cancer metabolism, facilitating lactate exchange and contributing to tumor aggressiveness. Their overexpression in various malignancies makes them attractive targets for both therapeutic and diagnostic strategies. In this study, we report the design, synthesis, and comprehensive characterization of a novel chimeric bioconjugate, L^{CPn}, integrating a coumarin-based MCT1-targeting moiety with a TACN(1,4,7-triazacyclononane)-containing chelator, optimized for copper radioisotope binding. The synthetic route was refined through strategic modifications, including mono-Boc (*tert*-butyloxycarbonyl) protecting group protection of the macrocycle and efficient SN_2-type coupling via thionyl chloride activation. Structural confirmation was achieved through nuclear magnetic resonance and mass spectrometry. Five protonation constants were determined for L^{CPn}, reflecting contributions from both the chelator and targeting domains. Complexation studies with Cu^{2+} and Zn^{2+} confirmed the formation of stable 1:1 metal-to-ligand complexes, while cyclic voltammetry studies indicated a quasi-reversible redox behaviour upon Cu^{2+} to Cu^{+} reduction. Docking simulations and cell-based assays demonstrated that the coumarin-based targeting moiety exhibits high affinity for MCT1 and effectively inhibits lactate uptake in prostate cancer models. These findings underscore the dual functionality of L^{CPn} as a selective MCT1-targeting agent and a robust copper-chelating platform, paving the way for future theranostics applications in oncology exploiting inorganic bioconjugates.

1. Introduction

Monocarboxylate Transporters (MCTs) encoded by the solute carrier family 16 (Slc16A) gene family are membrane proteins that through a proton-mediated mechanism facilitate the transport across cellular membranes of endogenous molecules such as lactate, pyruvate, ketone bodies and γ-hydroxybutyrate [1–3]. The MCT superfamily comprises 14 members but, so far, the attention of researchers has been focused mainly on MCT1 and MCT4, as they are known to maintain lactate homeostasis between oxidative and glycolytic cells under physiological conditions [1,2]. Once regarded merely as a metabolic waste product, lactate is now recognized as a key fuel in various cancer types, especially those with highly active oxidative phosphorylation (OXPHOS), where it can be preferred over glucose [4]. Its uptake and utilization affect cancer cell functions, including redox balance and angiogenesis. Tumors are often highly reliant on glycolytic metabolism, which promotes the overexpression of MCT1 and MCT4 transporters directly associated with enhanced proliferation, invasion, migration, and overall aggressiveness [5]. Overexpression of MCT1 and MCT4 was observed in breast, lung, stomach and colon and urological cancers [6–10]. Prostate cancer (PCa) is characterized by a peculiar metabolic adaptation, and high metabolic plasticity allows oxygenated cells to use glucose, glutamine, and lactate for bioenergic demands. A metabolic optimization in the tumor microenvironment (TME) allows oxidative PCa cells to use lactate from

☆ This article is part of a Special issue entitled: 'ISMEC24' published in Journal of Inorganic Biochemistry.

* Corresponding authors.
E-mail addresses: raphael.tripier@univ-brest.fr (R. Tripier), erika.ferrari@unimore.it (E. Ferrari).

https://doi.org/10.1016/j.jinorgbio.2025.113130
Received 4 August 2025; Received in revised form 20 October 2025; Accepted 22 October 2025
Available online 25 October 2025

stromal and hypoxic/glycolytic PCa cells [5,11]. Considering the role of MCT1 and MCT4 in cancer metabolism and the complexity of metabolic interactions within PCa cells, MCTs membrane proteins can be regarded as promising biological targets for new diagnostic and therapeutic strategies [12–14]. To date, several molecules (Fig. 1) have been tested as possible MCTs inhibitors able to induce apoptosis of cancer cells or to reduce cellular proliferation and invasion [13,15], including quercetin, diclofenac, cyano-cinnamic acid, BAY-8002 [13], AZD3965 [12] and 7ACC2 [12,13,16]. 7ACC2, a coumarin derivative, showed good inhibition of lactate influx into cells but almost no effects on lactate efflux. It was also found that this molecule inhibits the mitochondrial pyruvate transport, leading to an intracellular accumulation of pyruvate that hinders lactate uptake [12,13,16].

To date, AZD3965 has reached a Phase I study in patients with advanced cancer [17], however its molecular mechanisms still require to be clarified [14,18]. Despite targeting MCTs for therapy can be extremely challenging, these membrane proteins may be exploited as prognostic and diagnostic biomarkers. Recently, [^{18}F]-3-fluoro-2-hydroxypropionate has been tested for positron emission tomography (PET) imaging MCT-dependent lactate uptake in cancer cells [19], whereas a ^{11}C-labeled coumarin analogue was developed for detecting MCT expression [20]. The synthetic challenges associated with incorporating these fast decaying radioisotopes ($t_{1/2}$ 20.3 min and 109.8 min for ^{11}C and ^{18}F, respectively) into molecular skeleton greatly restrict their potential for clinical translation. A dual-functional molecule approach may overcome this limitation.

Dual-functional molecules have been used for medical purposes, and depending on the field of application, they are known under different names such as chimaeras, hybrids, bioconjugates, bifunctional compounds, multitargeting molecules, and engineered compounds [21]. The feature they all have in common is the general chemical structure that comprises a molecule able to target the biomarker that is linked through a spacer to an "effector" unit. This approach has been widely exploited in nuclear medicine, in which the "effector" part is a chelator bound to a radiometal and the "targeting" site is a biomolecule, typically a small molecule, peptide or antibody (Fig. S1) [22,23].

The use of radiometals facilitate the transition from diagnostic to therapeutic applications, enabling the integration of imaging and treatment in a single molecular platform, i.e. theranostics. Among metals for nuclear medicine applications, copper is earning a prominent attention being suitable for both imaging (^{60}Cu, ^{61}Cu, ^{62}Cu, ^{64}Cu) and targeted radiotherapy (^{64}Cu and ^{67}Cu)[23,24]. Particularly promising is ^{64}Cu (β^+ = 17.9 % (0.653 MeV); β^- = 38.4 % (0.579 MeV); EC = 43.1 %;) that can be considered a theranostics isotope with a moderate long-life ($t_{1/2}$ 12.7 h) suitable for PET imaging and therapy [25–27]. A wide number of acyclic and cyclic chelators have been investigated for selective and efficient binding of copper, among which azamacrocyles stand out for their thermodynamic stability (Fig. 2).

DOTA (1,4,7,10-tetraazacyclododecane-1,4,7,10-tetraacetic acid), considered "the" chelator in radiochemical clinical applications, forms a mononuclear complex characterized by distorted octahedral geometry in which Cu^{2+}sits above the plane defined by the four nitrogen atoms and the coordination sphere is completed by two opposite carboxylate groups [28]. The complex shows a quite high thermodynamic stability ($logK_{CuL}$ 22.2 [29]), similar to other cyclen derivatives such as DO2A2S (1,7-bis[2-(methylsulfanyl)ethyl]-4,10-diacetic acid-1,4,7,10-tetraaza cyclododecane – $logK_{CuL}$ = 22.0 [32]), DO2A2P (1,7-bis-methylene phosphonate-4,10-diacetic acid-1,4,7,10-tetraazacyclododecane - $logK_{CuL}$ = 24.90 [30]) and DO3A ((1,4,7,10-tetraazacyclododecane-1,4,7-triacetic acid - $logK_{CuL}$ = 25.75 [31]). Although the Cu^{2+} complex with NOTA (1,4,7-Triazacyclononane-1,4,7-triacetic acid) displays a thermodynamic stability comparable to that of DOTA ($logK_{CuL}$ = 23.33 [33]), competition exchange studies with [^{nat}Cu]Cu^{2+} on these chelators labeled with [^{64}Cu]Cu^{2+} demonstrated its superior kinetic inertness (100 % vs 5 % of intact complex for NOTA vs. DOTA at pH 7.5 [28]). This suggests that the enhanced imaging performance observed with NOTA over DOTA depends not on the thermodynamic stability but on the in vivo inertness [34,35]. One of the major challenges associated with Cu^{2+}-complexes in vivo is the potential for *demetallation* due the reduction of Cu^{2+} to Cu^{+} mediated by bio-reductive enzymes (such as reductases), glutathione or caused by the strongly hypoxic tumor microenvironment. Chelators capable of stabilizing both Cu(II) and Cu (I) oxidation states are particularly advantageous to address this issue, among them a TACN-based (1,4,7-triazacyclononane) chelator no3py characterized by pyridyl arms has been recently developed [36]. No3py chelator forms a highly thermodynamic stable Cu(II) complex ($\log K_{CuL}$ = 27.4) that exhibits a quasi-reversible redox process (E_{pc} = −742 mV, E_{pa} = −667 mV, ΔEp = 75 mV) [36], making it a promising candidate for in vivo uses.

The present study aims to design, synthesize and characterize a novel chimeric bioconjugate that combines a targeting vector based on 7ACC2 structure possessing high affinity for MCT1 and the no3py chelator,

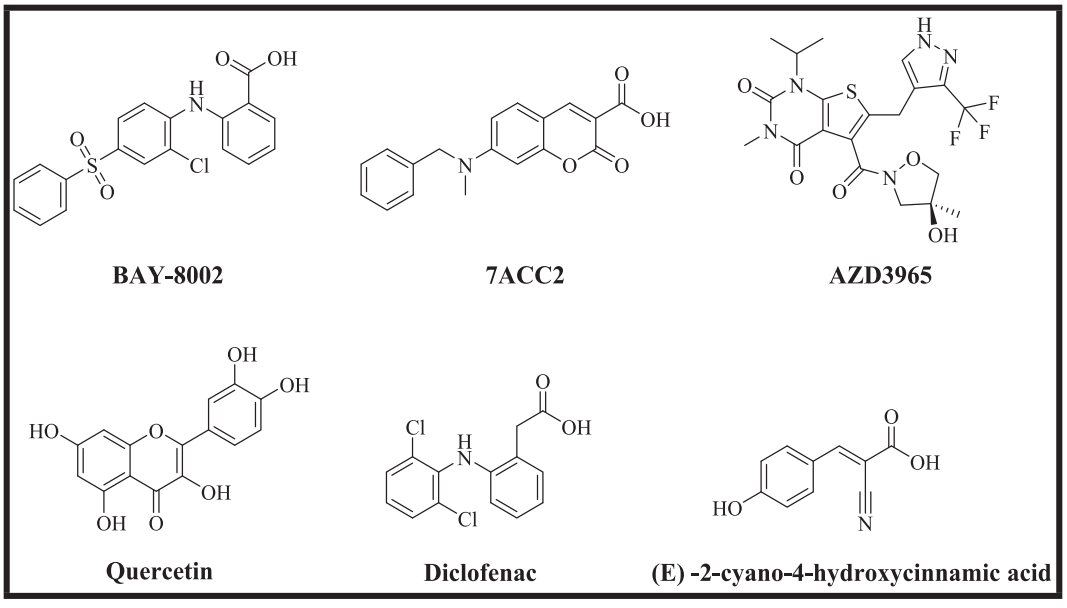

Fig. 1. MCT1 and MCT4 inhibitors.

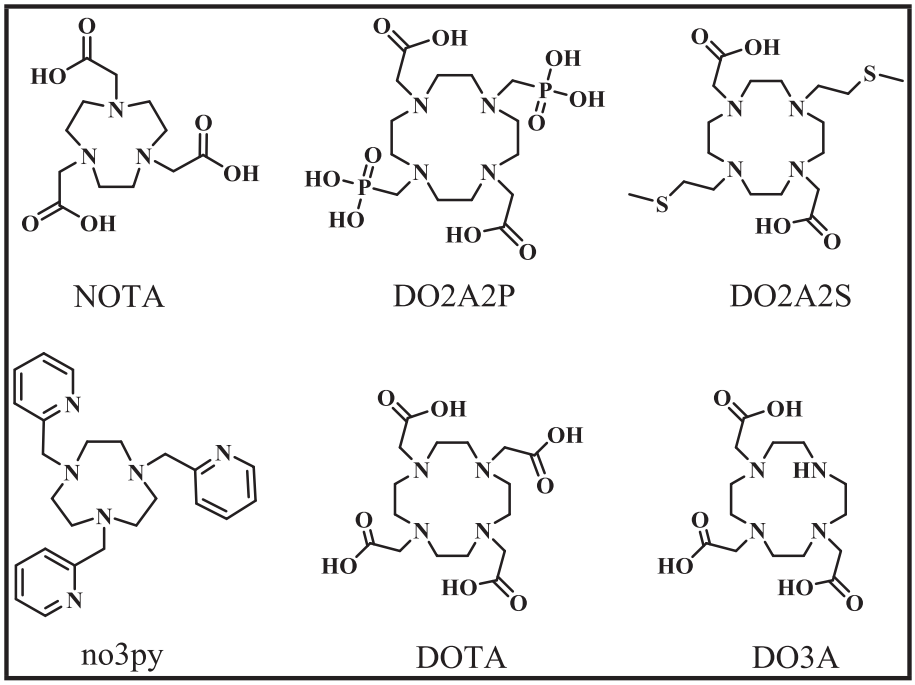

Fig. 2. TACN- and DOTA-based polyazamacrocycles for copper radioisotope chelation, for simplicity all chelators's names are reported in their short form that doesn't account for the number of acidic protons [28–31].

known for its strong and stable coordination of copper ions. In addition to the study of the Cu(II)/Cu(I) system, we have complemented the work by investigating the Zn(II) counterpart that allows for complementary methods of detection, particularly NMR spectroscopy.

The proposed molecular chimaera is designed as a potential platform for nuclear medicine applications, aiming to exploit the radioactive properties of copper radioisotopes for both diagnostic imaging and targeted radiotherapy in tumors overexpressing MCT1.

2. Experimental section

2.1. General

All chemicals were obtained from commercial suppliers and used as received without further purification. All solutions were prepared with ultrapure water (18.2 MΩ/cm) obtained from a Milli-Q Millipore system. Flash column chromatography was performed using silica gel (60 Å, 230–400 mesh, 40–63 μm, Sigma-Aldrich) and appropriate mobile phases, as described in the following section. NMR spectra were recorded on a Bruker Avance AMX 400 spectrometer (400.12 MHz ^{1}H; 100.13 MHz ^{13}C), Bruker Avance AMX 500 spectrometer (500 MHz ^{1}H; 126 MHz ^{13}C) or a Bruker Avance AMX 600 spectrometer equipped with a CryoProbe BBO H&F 5 mm in inverse detection (600.13 MHz ^{1}H, 150.13 MHz ^{13}C). All the spectra were acquired at 25 °C. Chemical shifts (δ) are reported in parts per million (ppm), referenced to the residual solvent peak in organic solvents or 3-(trimethylsilyl)propionic acid sodium salt (TSP) in D_2O. Coupling constants (J) are given in hertz (Hz). Atom numbering for NMR assignments refers to the Schemes displayed in the "Results and Discussion" Section. Complete ^{1}H/^{13}C NMR spectra are reported as Appendix I in Supporting Information. Mass spectra (MS) were carried out on an Agilent 6300 Ion Trap LC-MS system with an electrospray ionization (ESI) interface. Thermo Scientific™ FLASH 2000 CHNS Analyzer provided elemental analyses. UV–vis spectra were recorded on a JASCO V-770 UV/Vis/NIR spectrophotometer within the 200–800 nm spectral range, using quartz cells (1 cm optical path). Infrared spectra were recorded as ATR spectra using a Jasco FTIR4700LE or a Perkin Elmer FTIR-IRL1600300 spectrophotometer equipped with a diamond tip for solids and with a 2 cm^{-1} resolution; bands are reported as wavenumbers (cm^{-1}) together with their assignments and relative intensity (vs = very strong, s = strong, m = medium, w = weak, br = broad). Inductively coupled plasma mass spectra (ICP-MS) were acquired with the spectrometer iCAP TQ ICP-MSX (Thermo Fisher Scientific) equipped with Peltier cooled (3 °C) spray chamber. Samples were mineralized with sub-boiling HNO_3, diluted with Milli-Q water to a final concentration of 500–200 ppb and then introduced by the autosampler ESI SC-2 DX FAST into the nebulizer. Data were analysed by Qtegra software. The instrument was tuned daily with an ICP-MS tuning solution.

2.2. Synthesis

2.2.1. 7-Hydroxy-2-oxo-2H-1-benzopyran-3-carboxylic acid (1)

Compound **2** (501 mg, 2.14 mmol) was dissolved in 10 mL of methanol, LiOH was added (5 mL, 1 M in H_2O), and the solution was left under stirring at room temperature (RT) for 2 h. The organic phase was removed under reduced pressure and HCl 1 M was then added, forming a yellowish precipitate. The precipitate was filtered off, dried under reduced pressure and recrystallized from ethanol. The product was isolated as a yellow/brownish powder (yield 86 %). Elemental analysis for $C_{10}H_6O_5$ (g/mol): calc. C 58.26 %, H 2.93 %; exp. C 57.72 %, H 2.87 %. ESI-MS: m/z $[M-H]^-$: 204.8 (found); 205.01 (calc. for $C_{10}H_5O_5^-$). ^{1}H NMR (600 MHz, DMSO-d_6) δ 11.08 (s, 1H, -OH), 8.67 (d, J = 1.4 Hz, 1H, H-3), 7.74 (dd, J = 8.6, 1.7 Hz, 1H, H-5), 6.84 (ddd, J = 8.6, 2.3, 1.3 Hz, 1H, H-6), 6.73 (s, 1H, H-8). ^{13}C NMR (600 MHz, DMSO-d_6) δ 164.26 (C-7), 163.96 (C-1), 157.58 (C-9), 157.03 (C-10), 149.44 (C-3), 132.07 (C-5), 114.04 (C-6), 112.53 (C-2), 110.66 (C-4), 101.83 (C-8).

2.2.2. Ethyl 7-hydroxy-2-oxo-2H-1-benzopyran-3-carboxylate (2)

2,4 dihydroxybenzaldehyde (498 mg, 3.61 mmol) was dissolved in diethylmalonate (1.343 g, 8.39 mmol), then piperidine (365 mg, 4.29 mmol) was added as catalyst. The reaction was sonicated at RT for 1 h. 1 M HCl was added until acidic pH (4–5), confirming the neutralization of piperidine. The product was separated as a white solid by filtration, washed with distilled water and finally recrystallized from ethanol. The

product was isolated as white crystalline solid (yield 54 %). Elemental Analysis for $C_{12}H_{10}O_5 \cdot H_2O$ (252.20 g/mol): calc. C 57.1 %, H 4.80 %; exp. C 56.68 %, H 4.76 %. ESI-MS: *m/z* $[M\text{-}H]^-$: 233.2 (found); 233.04 (calc. for $C_{12}H_9O_5^-$).[1] H NMR (400 MHz, MeOD-d_4) δ 1.40 (3H, t, $J = 7.1$ Hz, -CH_3), 4.35 (2H, q, $J = 7.1$ Hz, -CH_2), 6.74 (1H, d, $J = 2.2$ Hz, H-8), 6.88 (1H, dd, $J = 8.6$, 2.3 Hz, H-6), 7.63 (1H, d, $J = 8.6$ Hz, H-5), 8.67 (1H, s, H-3). ^{13}C NMR (400 MHz, MeOD-d_4) δ 166.1 (C-7), 164.9 (C-1), 159.5 (C-9), 159.0 (C-10), 151.2 (C-3), 133.0 (C-5), 115.5 (C-6), 113.3 (C-2), 112.2 (C-4), 103.1 (C-8), 62.5 (-CH_2), 14.5 (-CH_3). FT-IR (ATR, cm^{-1}): 3541 m broad+3470 m broad (νO-H), 1735s + 1730s (νC=O_{ester}), 1299 m + 1144s (νC-O_{ester}), 1223 m (δOH), 842 s (δCH_{ar}), 796 s (ωCH_{aliph}).

2.2.3. Ethyl 7-{3-[(tert-butoxycarbonyl)amino]propoxy}-2-oxo-2H-1-benzopyran-3-carboxylate (3)

Compound **2** (433 mg 1.85 mmol) was dissolved in DMSO (5 mL) at 40–50 °C to form a yellow-green solution. When K_2CO_3 (252 mg, 1.83 mmol) and KI (142 mg, 0.858 mmol) were added, the solution turned dark. *Tert*-butyl (3-bromopropyl)carbamate (200 mg, 0.840 mmol) was dissolved in 3 mL of DMSO and added dropwise to the mixture. The solution was left under magnetic stirring at 50 °C for 3 days. The solution was cool down to RT, poured slowly into acid water (pH ~3) and the mixture was stirred for few minutes. The aqueous solution was extracted three times with ethyl acetate (EtOAc). The collected organic portions were washed with brine and dried with $MgSO_4$. After filtering off the solid, the solvent was removed under reduced pressure to give a yellow sticky-oily crude product that was suspended in water to form a white precipitate. The product was purified with alumina flash chromatography (DCM: EtOAc 100:0 ➔ 80:20 *v:v*). The product was isolated as white crystals (yield 48 %). Elemental Analysis for $C_{20}H_{25}NO_7$ (391.25 g/mol): calc. C 61.37 %, H 6.44 %, N 3.58 %; exp. C 61.08 %, H 6.49 %, N 3.68 %. ESI-MS: *m/z* $[M + H]^+$: 392.2 (found); 392.17 (calc. for $C_{20}H_{26}NO_7^+$); $[M\text{-}C_4H_9]^+$: 336.0 (found); 335.10 (calc. for $C_{16}H_{17}NO_7$). ^{1}H NMR (400 MHz, $CDCl_3$) δ 1.4 (t, $J = 7.1$ Hz, 3H, -CH_3), 1.4 (s, 9H, H-16), 2.0 (p, 2H, H-12), 3.3 (t, $J = 6.7$ Hz, 2H, H-13), 4.0–4.2 (t, 2H, H-11), 4.4 (q, $J = 7.1$ Hz, 2H, -CH_2), 4.7 (s, broad, 1H, -NH), 6.8 (d, $J = 2.3$ Hz, 1H, H-8), 6.9 (dd, $J = 8.7$, 2.4 Hz, 1H, H-6), 7.5 (d, $J = 8.7$ Hz, 1H, H-5), 8.5 (d, $J = 0.7$ Hz, 1H, H-3). ^{13}C NMR (600 MHz, $CDCl_3$) δ 164.5 (C-7), 163.6 (C-1), 157.6 (C-10), 157.3 (C-9), 156.1 (C-14), 149.1 (C-3), 130.9 (C-5), 114.3 (C-2), 114.0 (C-6), 111.8 (C-4), 101.0 (C-8), 79.6 (C-15) 66.6 (C-11), 61.8 (-CH_2), 37.8 (C-13), 29.6 (C-12), 28.5 (C-16), 14.4 (-CH_3). FT-IR (ATR, cm^{-1}): 3370 m (νN-H), 1750s + 1589s (νC=O_{ester}), 1683*vs* (νC=O_{amide}), 1553 m (νC-N), 1393w (νCH_3), 1226vs + 1124s (νC-O_{ester}), 1162s (νC_{ar}-O_{ether}), 1026s (νCH_2-O_{ether}), 868 s (νCH_{ar}).

2.2.4. 3-{[3-(ethoxycarbonyl)-2-oxo-2H-1-benzopyran-7-yl]oxy}propan-1-aminium (4)

Compound **3** (158 mg) was dissolved in 3 mL of dichloromethane (DCM). Trifluoroacetic acid (TFA) (1.0 mL) was added slowly, and the mixture sonicated for 45 min. The reaction was monitored by thin layer chromatography (TLC) (Petroleum Ether (EtPet):EtOAc 3:7 v:v). The solvent and residual TFA were removed under reduced pressure, the solid was washed with DCM for three times and then dried. The crude product (brown solid) was used without further purifications (yield 96 %). ESI-MS: *m/z* $[M + H]^+$: 291.9 (found); 292.12 (calc. for $C_{15}H_{18}NO_5^+$) ^{1}H NMR (600 MHz, DMSO-d_6) δ 1.3 (t, $J = 7.1$ Hz, 3H, -CH_3), 2.0 (p, $J = 6.4$ Hz, 2H, H-12), 3.0 (h, $J = 6.2$ Hz, 2H, H-13), 4.2 (t, $J = 6.1$ Hz, 2H, H-11), 4.3 (q, $J = 7.1$ Hz, 2H, -CH_2), 7.0 (dd, $J = 8.6$, 2.4 Hz, 1H, H-6), 7.0 (d, $J = 2.4$ Hz, 1H, H-8), 7.8 (s, 3H, -NH), 7.9 (d, $J = 8.7$ Hz, 1H, H-5), 8.7 (s, 1H, H-3). ^{13}C NMR (600 MHz, DMSO-d_6) δ 163.7 (C-7), 162.8 (C-1), 156.9 (C-10), 156.3 (C-9), 149.1 (C-3), 131.7 (C-5), 113.6 (C-6), 113.5 (C-2), 111.6 (C-4), 100.8 (C-8), 65.7 (C-11), 61.0 (-CH_2), 36.2 (C-13), 26.5 (C-12), 14.1 (-CH_3).

2.2.5. N-PEG-N-Boc-7-{3-[(tert-butoxycarbonyl)amino]propoxy}-2-oxo-2H-1-benzopyran-3-ethyl carboxylate (5)

Compound **4** (300 mg, 0.625 mmol) was dissolved in 3 mL of dry DMF together with Boc-15-amino-4,7,10,13-tetraoxapentadecanoic acid (214 mg, 0.586 mmol), HBTU (252 mg, 0.665 mmol) and DIPEA (1.1 mL, 6.31 mmol). The mixture was stirred overnight at RT. The crude was dissolved in DCM and extracted with NH_4Cl solution two times and one last time with brine. The product was purified with silica gel column chromatography (EtOAc ➔ EtOAc +5 % MeOH) and was obtained as a white sticky solid (yield 66 %). ESI-MS: *m/z* $[M\text{-}Boc]^+$: 539.4 (found); 539.26 (calc. for $C_{26}H_{39}N_2O_{10}^+$). ^{1}H NMR (500 MHz, $CDCl_3$) δ 1.4–1.5 (m, 12H, H-1 and H-24), 2.0 (p, $J = 6.5$ Hz, 2H, H-14), 2.5 (t, $J = 5.8$ Hz, 2H, H-17), 3.3 (t, $J = 5.1$ Hz, 2H, H-21), 3.4 (q, $J = 6.5$ Hz, 2H, H-15), 3.5 (t, $J = 5.2$ Hz, 2H, H-20), 3.6 (d, $J = 7.3$ Hz, 12H, H-19), 3.7 (t, $J = 5.7$ Hz, 2H, H-18), 4.1 (t, $J = 6.2$ Hz, 2H, H-13), 4.4 (q, $J = 7.1$ Hz, 2H, H-2), 6.8 (d, $J = 2.3$ Hz, 1H, H-7), 6.9 (dd, $J = 8.6$, 2.3 Hz, 1H, H-9), 7.5 (d, $J = 8.6$ Hz, 1H, H-10), 8.5 (s, 1H, H-12). ^{13}C NMR (151 MHz, $CDCl_3$) δ 14.4 (C-1), 28.6 (C-24), 29.1 (C-14), 36.4 (C-17), 37.1 (C-15), 40.5 (C-21), 61.8 (C-2), 66.8 (C-13), 67.4 (C-18), 70.3 (C-20), 70.4 (C-19), 70.4 (C-19′), 70.6 (C-19″), 70.7 (C-19‴), 70.7 (C-19⁗), 79.4 (C-23), 101.1 (C-7), 111.8 (C-11), 114.0 (C-9), 114.3 (C-4), 130.9 (C-10), 149.1 (C-12), 156.2 (C-22), 157.3, 157.7 (C-8), 163.6 (C-3), 164.5 (C-8), 172.0 (C-16).

2.2.6. N-PEG-7-{3-[(tert-butoxycarbonyl)amino]propoxy}-2-oxo-2H-1-benzopyran-3- Ethyl carboxylate (6)

Compound **5** (190 mg, 0.298 mmol) was dissolved in 3 mL of DCM and 1.0 mL of TFA was added. The mixture was then sonicated for 1 h. The product was then dried under reduced pressure. DCM was added and removed three times to remove traces of TFA. **6** was isolated as a white solid in quantitative yield. ESI-MS: *m/z* $[M + H]^+$: 539.5 (found); 539.26 (calc. for $C_{26}H_{39}N_2O_{10}^+$). ^{1}H NMR (500 MHz, MeOD-d_4) δ 1.4 (t, $J = 7.1$ Hz, 3H, H-1), 2.0 (p, $J = 6.4$ Hz, 2H, H-14), 2.5 (t, $J = 5.9$ Hz, 2H, H-17), 3.1 (t, $J = 5.1$ Hz, 2H, H-21), 3.4 (t, $J = 6.7$ Hz, 2H, H-15), 3.6–3.7 (m, 12H, H-19), 3.7–3.8 (m, 4H, H-18 and H-20), 4.2 (t, $J = 6.2$ Hz, 2H, H-13), 4.4 (q, $J = 7.1$ Hz, 2H, H-2), 6.9 (d, $J = 2.4$ Hz, 1H, H-7), 7.0 (dd, $J = 8.7$, 2.4 Hz, 1H, H-9), 7.7 (d, $J = 8.7$ Hz, 1H, H-10), 8.7 (s, 1H, H-12). ^{13}C NMR (126 MHz, MeOD-d_4) δ 172.8 (C-16), 165.0 (C-8), 163.3 (C-3), 157.8 (C-5), 157.4 (C-6), 149.4 (C-12), 131.2 (C-10), 113.9 (C-9), 111.7 (C-11), 100.4 (C-7), 69.9 (C-19), 69.5 (C-20), 66.9 (C-18), 66.4 (C-19′), 66.2 (C-13), 61.2 (C-2), 39.1 (C-21), 36.1 (C-17), 35.7 (C-15), 28.5 (C-14), 13.1 (C-1).

2.2.7. 10-phenyl-1,4,7-triazabicyclo[5.2.1]decane (7)

TACN (585 mg, 4.53 mmol) was dissolved in 50 mL of EtOH with molecular sieves and stirred for 30 min. Then benzaldehyde (0.46 mL, 4.37 mmol) was added. The mixture was left under magnetic stirring at RT overnight. The mixture was then filtered and dried. **7** was obtained as a white solid in quantitative yield. ESI-MS: *m/z* $[M]^+$: 216.3 (found); 216.15 (calc. for $C_{13}H_{18}N_3^+$). ^{1}H NMR (400 MHz, $CDCl_3$) δ 2.9–3.0 (m, 4H, Htacn), 3.0–3.0 (m, 2H, Htacn), 3.1–3.1 (m, 1H, Htacn), 3.1–3.1 (m, 1H, Htacn), 3.1–3.2 (m, 2H, Htacn), 3.3–3.4 (m, 2H, Htacn), 5.7 (s, 1H, H-4), 7.1–7.2 (m, 1H, H-8), 7.3–7.3 (m, 2H, H-7), 7.4–7.5 (m, 2H, H-6). ^{13}C NMR (101 MHz, $CDCl_3$) δ 145.6 (C-5), 128.0 (C-7), 126.6 (C-8), 126.5 (C-6), 88.3 (C-4), 58.7 (C-1), 49.5 (C-3), 49.1 (C-2).

2.2.8. tert-butyl 10-phenyl-1,4,7-triazabicyclo[5.2.1]decane-4-carboxylate (8i)

7 (3.05 mmol) was dissolved in 30 mL of DCM. TEA (1.1 mL, 7.91 mmol) was added. Di-*tert*-butyl carbonate (843 mg, 3.86 mmol) was dissolved in 20 mL of DCM and added dropwise to the first solution. Then the mixture was left stirring at RT overnight. The mixture was then dried under reduced pressure, giving a white-yellowish powder (purity 95 %). ESI-MS: *m/z* $[M + H]^+$: 318.2 (found); 318.22 (calc. for $C_{18}H_{28}N_3O_2^+$). ^{1}H NMR (400 MHz, $CDCl_3$) δ 1.5 (s, 9H, H-6), 3.0–3.3 (m, 8H, H-1/H-2), 3.5–3.8 (m, 4H, H-3), 5.2 (s, 1H, H-7), 7.2–7.2 (m, 1H, H-11), 7.3–7.3 (m, 2H, H-10), 7.5 (dt, $J = 8.0$, 1.2 Hz, 2H, H-9). ^{13}C NMR

(101 MHz, $CDCl_3$) δ 154.6 (C-4), 145.1 (C-8), 128.1 (C-10), 126.9 (C-11), 126.5 (C-9), 88.1 (C-7), 79.9 (C-5), 54.8 (C-1), 53.9 (C-1′), 49.4 (C-3), 49.2 (C-3′), 47.8 (C-2), 28.7 (C-6).

2.2.9. tert-Butyl 1,4,7-triazonane-1-carboxylate (8)

Benzaldehyde protection on **8i** was simply removed by performing column chromatography with alumina (DCM ➔ DCM + 10 % 7 M NH_3 in MeOH), giving the pure mono Boc-protected product. ESI-MS: *m/z* $[M + H]^+$: 230.2 (found); 230.33 (calc. for $C_{11}H_{24}N_3O_2^+$). ^{1}H NMR (400 MHz, $CDCl_3$) δ 1.4 (s, 9H, H-6), 2.7–2.9 (m, 4H, H-1), 3.0 (m, 4H, H-2), 3.3–3.4 (m, 4H, H-3), 4.0 (d, J = 9.3 Hz, 3H, NH_3). ^{13}C NMR (101 MHz, $CDCl_3$) δ 155.5 (C-4), 80.1 (C-5), 53.8 (C-3), 53.5 (C-3′), 48.1 (C-1), 48.1 (C-1′), 48.0 (C-2), 47.2 (C-2′), 28.5 (C-6).

2.2.10. tert-Butyl 4, 7-dibenzyl-1,4,7-triazonane-1-carboxylate (9)

8 (567 mg, 2.47 mmol) was dissolved in 50 mL of dry ACN. K_2CO_3 (1.705 g, 12.35 mmol) and KI (965 mg, 5.81 mmol) were added and the resulting mixture was stirred at RT for 30 min. Then 2-(chloromethyl) pyridine hydrochloride (958 mg, 5.84 mmol) was added. The solution was left under magnetic stirring at RT for 3 days. Then, the solvent was removed under reduced pressure. The obtained solid was triturated with DCM to recollect the product and filtered. The organic phase was dried under reduced pressure. The crude product was purified with alumina chromatography (Hex/EtOAc 1:1 to EtOAc +5 % MeOH) and then isolated as a yellow oil (yield 67 %). ESI-MS: *m/z* $[M + H]^+$: 411.9 (found); 412.27 (calc. for $C_{23}H_{34}N_5O_2^+$). ^{1}H NMR (600 MHz, $CDCl_3$) δ 1.4 (d, J = 1.7 Hz, 9H, H-12), 2.6–2.6 (m, 2H, H-2/3), 2.7–2.7 (m, 2H, H-2/3), 2.9 (m, 2H, H-2/3), 3.0–3.1 (m, 2H, H-2/3), 3.3–3.4 (m, 4H, H-1), 3.8 (d, J = 4.7 Hz, 3H, H-4), 7.1 (m, 2H, H-8), 7.5 (m, 2H, H-6), 7.6 (m, 2H, H-7), 8.5–8.5 (m, 2H, H-9). ^{13}C NMR (151 MHz, $CDCl_3$) δ 28.7 (C-12), 49.9 (C-1), 50.4 (C-1′), 54.1 (C-2/3), 54.6 (C-2/3), 55.3 (C-2′3′), 56.5 (C-2′3′), 63.8 (C-4), 64.0 (C-4′), 79.4 (C-11), 122.0 (C-8), 122.0 (C-8′), 123.2 (C-6), 123.3 (C-6′), 136.5 (C-7), 136.5 (C-7′), 149.0 (C-9), 149.1 (C-9′), 155.7 (C-10), 160.3 (C-5), 160.3 (C-5′).

2.2.11. 1,5-Di[(pyridin-2-yl)methyl]-1,5,9-triazacyclononane (10)

9 (183 mg, 0.445 mmol) was dissolved in 3 mL of DCM. 1 mL of TFA was then added and the mixture was sonicated for 1 h. The product was then dried under reduced pressure. DCM was added and evaporated three times to remove traces of TFA. The product was then dissolved in water, pellets of KOH were added up to a pH of 13. Then the water phase was extracted with DCM four times. The organic fractions were collected and dried with $MgSO_4$. The mixture was then filtered, and the solvent removed under pressure to provide **9** as a yellow oil in quantitative yield. ESI-MS: *m/z* $[M + H]^+$: 312.2 (found); 312.22 (calc. for $C_{18}H_{26}N_5^+$). ^{1}H NMR (500 MHz, $CDCl_3$) δ 2.7 (s, 4H, H-3), 2.9–3.0 (m, 4H, H-2), 3.1–3.3 (m, 4H, H-1), 3.9 (s, 4H, H-4), 7.2–7.2 (m, 4H, H-6 and H-8), 7.6 (td, J = 7.7, 1.8 Hz, 2H, H-7), 8.6–8.7 (m, 2H, H-9). ^{13}C NMR (126 MHz, $CDCl_3$) δ 158.2 (C-5), 149.6 (C-9), 136.9 (C-7), 122.9 (C-6/8), 122.7 (C-6/8), 61.0 (C-4), 53.1(C-3), 49.7 (C-2), 45.5 (C-1).

2.2.12. Methyl 6-[2-(hydroxymethyl)pyridin-4-yl]hex-5-ynoate (11)

The experimental conditions were adapted from palladium-copper catalyzed Sonogashira reaction [37]. 10 mL of distilled TEA and 10 mL of distilled THF were mixed in a Schlenk tube. (4-Bromopyridin-2-yl) methanol (1.065 g, 5.664 mmol) and methyl hex-5-ynoate (1.023 g, 7.084 mmol) were added and the mixture was frozen, degassed and thawed three times. Then metal catalysts were added under nitrogen flux. The mixture was then heated to 55 °C and stirred for 18 h. The solvent was then removed under reduced pressure and the mixture was retaken in DCM, washed two times with a solution of NH_4Cl and brine. The remaining organic phase was dried with $MgSO_4$, filtered and the solvent removed under reduced pressure. The crude black oil was purified with silica gel flash chromatography: Hexane/EtOAc (8:2 *v*:v) ➔ EtOAc. Compound **11** was collected as a brown oil (yield 63 %). ESI-MS: *m/z* $[M + H]^+$: 234.1 (found); 234.11 (calc. for $C_{13}H_{16}NO_3^+$). ^{1}H NMR (400 MHz, $CDCl_3$) δ 1.9 (p, J = 7.2 Hz, 2H, H-4), 2.5 (td, J = 7.2, 5.0 Hz, 4H, H-3 and H-5), 3.4 (s broad, 1H, -OH), 3.7 (s, 3H, H-1), 4.7 (s, 2H, H-13), 7.1–7.2 (m, 1H, H-12), 7.2 (s, 1H, H-9), 8.4 (d, J = 5.1 Hz, 1H, H-11). ^{13}C NMR (101 MHz, $CDCl_3$) δ 173.5 (C-2), 159.4 (C-10), 148.5 (C-11), 132.8 (C-8), 124.6 (C-9), 122.8 (C-12), 94.6 (C-6), 79.3 (C-7), 64.2 (C-13), 51.8 (C-1), 32.9 (C-3), 23.6 (C-4), 19.0 (C-5).

2.2.13. Methyl 6-[2-(chloromethyl)pyridin-4-yl]hex-5-ynoate (12)

11 (502 mg, 2.15 mmol) was dissolved in 10 mL of DCM. Thionyl chloride (0.18 mL, 2.48 mmol) was dissolved in 10 mL of DCM and slowly dropped in the first solution. The reaction was monitored by TLC (Hex/EtOAc 1:1 *v:v*). After 60 min the mixture was washed two times with saturated $NaHCO_3$ solution and brine. The remaining organic phase was dried with $MgSO_4$, filtered and the solvent removed under reduced pressure obtaining a dark red oil. The crude product was purified with silica gel chromatography: Hex ➔ Hex/EtOAc (1:1 *v:v*). 12 was obtained as a yellow oil (yield 77 %). ESI-MS: *m/z* $[M + H]^+$: 252.3 (found); 252.08 (calc. for $C_{13}H_{15}ClNO_2^+$). ^{1}H NMR (400 MHz, $CDCl_3$) δ 1.9 (p, J = 7.1 Hz, 2H, H-4), 2.5–2.6 (m, 4H, H-3 and H-5), 3.7 (s, 3H, H-1), 4.6 (s, 2H, H-13), 7.2 (dd, J = 5.1, 1.5 Hz, 1H, H-12), 7.4 (s, 1H, H-9), 8.5 (dd, J = 5.1, 0.9 Hz, 1H, H-11). ^{13}C NMR (101 MHz, $CDCl_3$) δ 173.5 (C-2), 156.7 (C-10), 149.4 (C-11), 133.3 (C-8), 125.2 (C-9), 125.0 (C-12), 95.1 (C-6), 79.1 (C-7), 51.8 (C-1), 46.5 (C-13), 32.9 (C-3), 23.6 (C-4), 19.1 (C-5).

2.2.14. no3pyCOOMe (13)

10 (311 mg, 0.445 mmol) was dissolved in 25 mL of dry ACN. K_2CO_3 (0.509 g, 3.69 mmol) was added, and the suspension was left under magnetic stirring for 30 min. **12** (206.2 mg, 0.820 mmol) was dissolved in 10 mL of dry ACN and added to the first solution. The mixture was left under magnetic stirring at RT for 72 h. The solvent was removed, and the mixture was washed with DCM to recollect the product. The solvent was removed and the crude purified with column chromatography with alumina (III) (DCM ➔ DCM + 4 % MeOH). **13** was isolated as a brown oil (yield 66 %). ESI-MS: m/z $[M + H]^+$: 526.7 (found); 527.31 (calc. for $C_{31}H_{39}N_6O_2^+$). ^{1}H NMR (500 MHz, $CDCl_3$) δ 1.9 (p, J = 7.2 Hz, 2H, H-4), 2.5 (q, J = 7.1 Hz, 4H, H-3 and H-5), 2.9 (s, 12H, H_{tacn}), 3.7 (s, 3H, H-1), 3.7–4.0 (m, 6H, H-13 and H-17), 7.1–7.1 (m, 1H, H-12), 7.2 (t, J = 6.4 Hz, 2H, H-21), 7.5 (s, 1H, H-9), 7.5 (d, J = 7.8 Hz, 2H, H-19), 7.6 (td, J = 7.6, 1.8 Hz, 2H, H-20), 8.4 (dd, J = 5.2, 0.8 Hz, 1H, H-11), 8.5–8.5 (m, 2H, H-22). ^{13}C NMR (151 MHz, $CDCl_3$) δ 19.1 (C-5), 23.6 (C-4), 32.9 (C-3), 50.7 (2xC_{taCn}), 51.3 (C_{taCn}), 51.8 (C-1), 60.6 (C-17), 61.0 (C-13), 79.1 (C-7), 95.8 (C-6), 123.5 (C-21), 124.9 (C-19), 125.3 (C-12), 126.1 (C-9), 133.4 (C-8), 137.7 (C-20), 149.1 (C-22), 149.2 (C-11), 155.0 (C-18), 156.4 (C-10), 173.4 (C-2).

2.2.15. no3pyCOOK (14)

13 (155 mg, 0.294 mmol) was dissolved in 10 mL of THF and 1.0 mL of KOH 1.0 M was added. The solution was heated at 50 °C overnight. Then the solvent was removed under reduced pressure. The crude product (brown oil) was obtained in quantitative yield and used without further purification. ESI-MS: *m/z* $[M + H]^+$: 512.8 (found); 513.30 (calc. for $C_{30}H_{37}N_6O_2^+$). ^{1}H NMR (400 MHz, D_2O) δ 1.8 (p, J = 7.1 Hz, 2H, H-3), 2.4 (t, J = 7.4 Hz, 2H, H-2), 2.5 (t, J = 6.9 Hz, 2H, H-4), 3.0–3.1 (m, 12H, H-13, H-14 and H-15), 4.1 (s, 2H, H-12), 4.3 (s, 4H, H-16), 7.5 (dd, J = 5.5, 1.6 Hz, 1H, H-8), 7.6 (ddd, J = 7.8, 5.3, 1.2 Hz, 2H, H-20), 7.7–7.8 (m, 3H, H-18 and H-11), 8.1 (ddd, J = 7.8, 1.7 Hz, 2H, H-19), 8.3 (dd, J = 5.5, 0.7 Hz, 1H, H-10), 8.5 (ddd, J = 5.3, 1.7, 0.8 Hz, 2H, H-21). ^{13}C NMR (151 MHz, D_2O) δ 179.1 (C-1), 154.7 (C, 152.7, 146.9 (C-21), 146.2 (C-10), 141.8 (C-19), 135.8, 126.8 (C-8), 126.3 (C-11), 125.8 (C-18), 125.0 (C-20), 99.2 (C-5), 78.5 (C-6), 58.9 (C-12), 58.0 (C-16), 49.5 (C_{taCn}), 49.0 (C_{taCn}), 48.8 (C_{taCn}), 33.6 (C-2), 23.1 (C-3), 18.4 (C-4).

2.2.16. L^{CPn}Me (15)

Compound **6** (0.294 mmol) was dissolved in 3 mL of dry DMF together with compound **14** (0.298 mmol), HBTU (125.61 mg, 0.331

mmol) and DIPEA (371 mg, 2.87 mmol). The mixture was stirred at RT overnight. The solvent was removed under reduced pressure and the crude product was dissolved in DCM and extracted with brine. The product was dissolved in hot ethanol (EtOH), then let cool down and separated from the solid. EtOH was removed under reduced pressure and **15** isolated as a yellow oil (yield 30 %). ESI-MS: *m/z* $[M + H]^+$: 1033.6 (found); 1033.54 (calc. for $C_{56}H_{73}N_8O_{11}^+$); $[M + 2H]^{2+}$: 517.6 (found); 517.78 (calc. for $C_{56}H_{74}N_8O_{11}^{2+}$). ^{1}H NMR (400 MHz, $CDCl_3$) δ 1.3 (td, $J = 7.1$, 2.7 Hz, 3H, H-42), 1.9 (qt, $J = 7.2$, 3.5 Hz, 2H, H-19), 2.0 (pd, $J = 6.4$, 2.2 Hz, 2H, H-29), 2.3 (td, $J = 7.4$, 2.5 Hz, 2H, H-18), 2.4 (td, $J = 6.8$, 6.4, 2.3 Hz, 4H, H-20 and H-26), 3.0 (d, $J = 7.2$ Hz, 12H, H-1,2 and 3), 3.4 (pd, $J = 6.1$, 5.7, 2.5 Hz, 4H, H-22 and H-28), 3.5 (td, $J = 5.5$, 2.2 Hz, 2H, H-23), 3.6 (t, $J = 3.2$ Hz, 12H, H-24), 3.7 (td, $J = 5.9$, 2.1 Hz, 2H, H-25), 4.0 (d, $J = 3.5$ Hz, 2H, H-10), 4.0–4.1 (m, 6H, H-4 and H-30), 4.3 (qd, $J = 7.0$, 3.0 Hz, 2H, H-41), 6.5 (q, $J = 6.1$ Hz, 1H, -NH no3py), 6.7 (t, $J = 2.9$ Hz, 1H, H-39), 6.9 (ddd, $J = 8.6$, 2.7 Hz, 2H, H-32 and –NH coumarin), 7.1 (dt, $J = 4.1$, 1.8 Hz, 1H, H-14), 7.2–7.2 (m, 2H, H-8), 7.4 (dd, $J = 7.7$, 2.6 Hz, 2H, H-6), 7.4 (d, $J = 2.7$ Hz, 1H, H-12), 7.5 (dd, $J = 8.7$, 1.7 Hz, 1H, H-33), 7.6 (ddd, $J = 7.6$, 2.1 Hz, 2H, H-7), 8.3 (dd, $J = 5.2$, 2.4 Hz, 1H, H-15), 8.4–8.5 (m, 3H, H-9 and H-35). ^{13}C NMR (101 MHz, $CDCl_3$) δ 172.4 (C-21), 171.9 (C-27), 164.6 (C-31), 163.2 (C-40), 157.4 (C-37/38), 157.3 (C-37/38), 155.8 (C-11), 155.0 (C-5), 149.4 (C-9), 149.2 (C-15), 149.1 (C-35), 137.3 (C-7), 133.2 (C-13), 130.9 (C-33), 125.9 (C-12), 125.2 (C-14), 124.0 (C-6), 123.3 (C-8), 113.9 (C-32), 113.7 (C-36), 111.6 (C-34), 101.0 (C-39), 96.1 (C-17), 78.7 (C-16), 70.4 (C-24), 70.4 (C-24′), 70.2 (C-24″), 70.1 (C-24‴), 69.7 (C-24⁗), 67.2 (C-25), 66.7 (C-30), 61.6 (C-41), 60.2 (C-10), 60.0 (C-4), 50.1 (C-1/2/3), 49.7 (C-1/2/3), 49.6 (C-1/2/3), 39.2 (C-22), 36.9 (C-26), 36.2 (C-28), 34.9 (C-20), 28.9 (C-29), 24.1 (C-19), 19.0 (C-18), 14.3 (C-43).

2.2.17. L^{CPn} (16)

Compound **15** (121 mg, 0.117 mmol) was dissolved in 2 mL of MeOH, then 1.0 mL of 1 M LiOH was added and the solution was left under magnetic stirring at RT for 30 min. MeOH was then removed under reduced pressure. The crude product was purified with semi-preparative HPLC: H_2O: ACN (95:5 *v/v*) ➔ H_2O: ACN (10:90 *v/v*). $\mathbf{L^{CPn}}$ was collected as a yellow solid (yield 34 %). Elemental Analysis for $LiC_{54}H_{67}N_8O_{11}$ (1011.13 g/mol): calc. C 64.15 %, H 6.68 %, N 11.08 %; exp. C 63.98 %, H 6.80 %, N 10.93 %. ESI-HRMS: *m/z* $[M + H]^+$: 1005.5082 (found); 1005.5080 (calc. for $C_{54}H_{69}N_8O_{11}^+$); $[M + 2H]^{2+}$: 503.2579 (found); 503.2576 (calc. for $C_{54}H_{70}N_8O_{11}^{2+}$). ^{1}H NMR (400 MHz, MeOD-d_4) δ 1.9 (p, $J = 7.2$ Hz, 2H, H-19), 2.0 (p, $J = 6.4$ Hz, 2H, H-29), 2.4 (t, $J = 7.4$ Hz, 2H, H-18), 2.4 (t, $J = 6.0$ Hz, 2H, H-26), 2.5–2.5 (m, 2H, H-20), 3.0 (d, $J = 10.9$ Hz, 12H, H-1, H-2 and H-3), 3.4 (t, $J = 5.6$ Hz, 2H, H-22), 3.4 (t, $J = 6.6$ Hz, 2H, H-28), 3.5 (t, $J = 5.5$ Hz, 2H, H-23), 3.6–3.6 (m, 12H, H-24), 3.7 (t, $J = 6.0$ Hz, 2H, H-25), 4.1–4.2 (m, 8H, H-4, H-10, H-30), 6.9 (d, $J = 2.4$ Hz, 1H, H-39), 6.9 (dd, $J = 8.6$, 2.4 Hz, 1H, H-32), 7.3 (dd, $J = 5.2$, 1.6 Hz, 1H, H-14), 7.4 (ddd, $J = 7.6$, 4.9, 1.2 Hz, 2H, H-8), 7.5–7.6 (m, 3H, H-33 and H-6), 7.7 (s, 1H, H-12), 7.8 (td, $J = 7.7$, 1.8 Hz, 2H, H-7), 8.1 (s, 1H, H-35), 8.4 (dd, $J = 5.1$, 0.8 Hz, 1H, H-15), 8.5–8.6 (m, 2H, H-9). ^{13}C NMR (126 MHz, MeOD-d_4) δ 175.2 (C-21), 174.2 (C-27), 171.1 (C-40), 164.1 (C-31), 161.1 (C-37), 158.1 (C-11), 157.3 (C-38), 156.6 (C-5), 150.3 (C-9), 150.2 (C-15), 144.1 (C-35), 138.8 (C-7), 134.8 (C-13), 131.1 (C-33), 127.1 (C-12), 126.4 (C-14), 125.4 (C-6), 124.6 (C-8), 124.5 (C-36), 114.3 (C-32), 113.9 (C-34), 101.8 (C-39), 97.0 (C-17), 79.0 (C-16), 71.5 (C-24″), 71.4 (C-24′), 71.2 (C-24), 70.5 (C-23), 68.3 (C-25), 67.3 (C-30), 61.7 (C-10), 61.2 (C-4), 51.2 (C_{TACN}), 50.8 (C_{TACN}), 40.4 (C-22), 37.8 (C-26), 37.2 (C-28), 35.9 (C-18), 29.9 (C-29), 25.8 (C-19), 19.7 (C-20).

2.3. Docking and modelling

Molecular docking was performed using the Glide programme within the Maestro 13.4 Molecular modelling Suite from Schrödinger, LLC, New York, NY. The X-ray crystal structures of MCT1 in its inward-open and outward-open conformations were obtained from the RCSB PDB databank https://www.rcsb.org (PDB code 7CKO and 7CKR respectively). The protein structures were prepared according to the standard protein preparation workflow of Maestro, which includes adding hydrogen atoms, completing the missing loops, and assigning force field parameters. The grids were generated using the Receptor Grid Generation module using the centroid of the co-crystallized ligand (7ACC2 for 7CKO, BAY-8002 for 7CKR) as center of the grid box; the box was set as a cube with a 10 A side. The docked compounds were prepared using the LigPrep module of Maestro using the PLS-2004 force field to generate ionization states at pH 7.0 ± 2.0, and multiple conformers of each compound. All molecules were then docked using XP precision, and the results visualised with PyMol (www.pymol.org). The putative length of the PEG linker chain was evaluated using the 3D Builder utility of the suite.

2.4. Cell lines

Cancer DU145 (ATCC Cat# HTB-81) and LNCaP (ATCC Cat# CRL-1740) were grown in RPMI 1640 Medium. Cancer PC3 cells (ATCC Cat# CRL-1435) were maintained in Ham's F12 Medium. All media (Biowest) were supplemented with 2 mM glutamine, 100 IU/mL penicillin, 100 µg/mL streptomycin and 10 % FBS (Gibco). Normal RWPE1 (ATCC Cat# CRL-11609) were grown in Keratinocyte Serum Free Medium (K-SFM; # 17005042, Gibco), supplemented with 0.05 mg/mL bovine pituitary extract (Gibco) and 5 ng/mL human recombinant epidermal growth factor (Gibco). Normal primary PrEC epithelial cells (ATCC Cat# PCS-440-010) were grown in a serum-free Prostate Epithelial Cell Basal Medium (#PCS-440-030, ATCC) supplemented with Prostate Epithelia Cell Growth Kit (#PCS-440-040, ATCC). According to manufacturer's protocol, PrEC cells were not used beyond 10 passages. All cells were grown at 37 °C in a humidified incubator containing 5 % CO_2. All above-mentioned cell lines were verified to be mycoplasma free (EZ-PCR Mycoplasma Test Kit (Biological Industries, Connecticut, USA; #20–700-20) and passaged <3 months. All cells were grown at 37 °C in a humidified incubator containing 5 % CO_2.

2.5. Cell treatments and cell viability

1×10^4 LNCaP cells were seeded into 48-well plate and the following day they were treated with compound **1** at 30 µM concentration, in complete growth medium or in medium w/o glucose and w/o glutamine (#D9800–02, US Biological), supplemented with 3.7 g/L sodium bicarbonate and 10 mM lactic acid (#D9800–02, US Biological). After 72 h, PrestoBlue reagent (#A13261, Thermo Fisher Scientific) was added to the medium (1:9 *v/v*) and incubated for 1 h at 37 °C. Cell viability was calculated via PrestoBlue reduction levels by analyzing absorbance data obtained at 570–620 nm, according to the manufacturer's protocol.

A functional 3-bromopyruvate (3BP) cytotoxicity assay was performed as described in the literature [38], with minor modifications. LNCaP and PC3 cells were pre-treated for 6 h with compound 1 (30 µM; 10 µM) or with the reference MCT1 inhibitor 7ACC2 (100 µM; 50 µM; 10 µM). 3BP (LNCaP) or 70 µM (PC3) was then administered to LNCaP cells for 16 h, together with compound **1** or 7ACC2 at the same concentrations used in the pre-treatment. As reference, all compounds were also administered as a single agent in all performed experiments. Protection of LNCaP cells from the cytotoxic effect of 3BP was evaluated by measurement of cell viability as described above (PrestoBlue cell viability reagent).

2.6. RNA extraction and qRT-PCR analysis

RNA was purified from cell lines by using Ripospin II mini Kit (#314–150, GeneAll), according to the manufacturer's protocol. 200 ng of RNA was retrotranscribed with PrimeScript RT Reagent Kit (#RR037A, Takara Bio) and quantitative real-time PCR was performed with SsoAdvanced Universal SYBR Green Supermix (#1725274, Bio-

Rad, USA) using Biorad CFX connect Real-Time PCR Detection System. Oligonucleotides specific for Slc16a1/MCT1 (F: gccctgtgttcctctgtact; R: ccagctttctcaagggatgc) and RPS20 (F: gcgcctcttatcaagtcagc; R: cggaaaaacacccgtggag) were used. Data were analysed using the Bio-Rad CFX Maestro 2.0 software (Bio-Rad) and mRNA expression was normalized to Rps20. Data are expressed as relative expression compared to RWPE1, arbitrary set at 1.

2.7. Protein extraction and immunoblotting

Whole-cell protein extracts were prepared by lysis of control or treated-cells into 1× SDS sample buffer (25 mM Tris–HCl pH 6.8, 1.5 mM EDTA, 20 % glycerol, 2 % SDS, 5 % β-mercaptoethanol). Equivalent amounts of cellular extracts were resolved by SDS-PAGE, transferred to nitrocellulose membrane with Trans-Blot Turbo Transfer System (Bio-Rad) and immunoblotted with the following primary antibodies, diluted 1:1000 in 1× TBS with 1 mg/mL BSA: anti-βActin (#66009, Proteintech Europe) and anti-MCT1 (#*E*-AB-53264, Elabscience). Membranes were blotted and scanned with an Amersham Imager AI680 RGB (GE Healthcare), using NeoPRO Pico PLUS detection reagent (NeoBiotech).

2.8. TCGA data analysis

Expression levels of Slc16a1/MCT1 were evaluated based on RNA-seq data of the TCGA- Prostate Adenocarcinoma (PRAD) dataset. The box plot of Slc16a1 expression was obtained using Gene Expression Profiling Interactive Analysis - GEPIA2 (http://gepia2.cancer-pku.cn/, accessed on July 29th, 2025) [doi: https://doi.org/10.1093/nar/gkz430], an interactive web server for analyzing the RNA sequencing expression data of tumors and normal samples from the TCGA and the GTEx projects using a standard processing pipeline.

2.9. Copper uptake in cells

60.000 cells (PC3 and RWPE-1) were seeded into 12-well plates and treated with [CuL^{CPn}] complex in water (50 μM, 24 h incubation time). After the incubation time, the cells were washed twice with PBS and cell pellets were frozen and stored at −80 °C. The cell pellets were digested for 24 h in 200 μL of ultrapure HNO_3 65 % *w*/w, obtained from analytical grade HNO_3 (Carlo Erba, Milan, Italy) after sub-boiling distillation performed with a sub-boiler SAVILLEX DST 1000 (Savillex Corp. USA) apparatus. The resulting solutions were diluted up to a total mass of 6 g with Milli-Q water in 15 mL polypropylene tubes and analysed for their Cu content. The collected samples were randomly acquired using the inductively coupled plasma mass spectrometer iCAP TQ ICP-MSX (Thermo Fisher Scientific) equipped with Peltier cooled (3 °C) spray chamber. Samples were introduced by the autosampler ESI SC-2 DX FAST into the nebulizer, and the positively charged ions were then produced by a high-temperature, inductively coupled plasma. Data were analysed by Qtegra software. The instrument was tuned daily with an ICP-MS tuning solution. Y in HNO_3 2 % (100 ppb) was used as internal standard. Cu standard solutions ranging from 0.1 to 100 ppb were freshly prepared before each analysis and used to build the calibration curve. Two replicates of each experiment were carried out. Each sample was analysed at least in 2 independent measurements and each measurement is the average of 5 repetitions. Results are given as mean value ± standard deviation.

2.10. Statistical analysis

Statistical analyses of qPCR and cell viability data were performed using GraphPad PRISM 9.0 software (GraphPad Prism), using one-sample *t*-test or two-way ANOVA with post-hoc tests, as specified in the figure legends. Graphs represent Means ± Standard Error of the Mean (SEM). Data are considered to be statistically significant if $p < 0.05$ (*), $p < 0.01$ (**), $p < 0.001$ (***) and $p < 0.0001$ (****).

2.11. NMR and UV–vis spectroscopy

^{1}H NMR titrations were performed on a 4 mM solution of L^{CPn} in D_2O at 25 °C. Trimethylsilylpropanoic acid (TSP) was added as a reference compound ($\delta = 0$ ppm). The pD was measured directly with a pHmeter calibrated with commercial buffers at pH 7.0 and 4.0. The pD measured was then converted in the corresponding pH value through the 0.41 correction, to account for isotopic effects [39]. Spectra were acquired suppressing H_2O signal with Bruker "*zgcppr*" pulse sequence. After each acquisition, the pH was modified with CO_2-freed NaOD or DCl to collect ^{1}H NMR spectra in the range 2–10. NaCl (0.1 M) was used to keep the ionic strength constant.

UV–visible spectra were recorded at 25 °C in a 250–800 nm spectral range employing quartz cells (1 cm optical path). A stock solution of the ligand was prepared dissolving 4 mg of compound in 1 mL of ultrapure water and stored at 4 °C ($C_L = 3.98$ mM). The analysed L^{CPn} solution was prepared by diluting the right amount of stock solution in NaCl (0.1 M) to the final concentration of 0.1 mM. The initial pH of the solution was measured, and the spectrum acquired. Then, the pH of the solution was changed through negligible addition of concentrated HCl and NaOH solutions (<1 μL) to keep the total volume constant. Spectra were acquired at each pH variation. pH measurements were performed using a calibrated pH meter (Mettler-Toledo).

Stock solutions of L^{CPn} and Cu^{2+} were combined in metal-to-ligand 1-to-1 molar ratio ($C_{Cu} = C_L = 100$ μM; $I = 0.10$ M NaCl) and pH was changed similarly to free ligand solution by addition of small volumes (μL) of HCl and/or NaOH. The electronic spectra were recorded, and the equilibrium was considered to be reached when no further changes in either the pH or the electronic spectra were observed over time.

The spectroscopic data were elaborated with HypSpec, HypNMR or as described in previous publications [40–42]. Hydrolysis constants and solubility products of Cu^{2+} in aqueous ionic media were taken from ref. [43].

2.12. Cyclic voltammetry

All electrochemical measurements were performed using an Autolab PGSTAT-30 (Eco Chemie, Utrecht, The Netherlands) potentiostat/galvanostat, under the control of GPES software. Voltammetric measurements, namely cyclic voltammetry (CV), were performed in a conventional three electrode cell composed of glassy carbon (GC) as the working electrode (Metrohm), Pt wire as the counter-electrode, and Ag/AgCl/KCl 3 M (Amel) as the reference electrode. GC electrode was cleaned by mechanical abrasion with 0.05 μm alumina powder and washed in ethanol/water solution before use.

Voltammetric measurements were performed at 25 °C starting from 0.0 V with the first vertex at −0.2/−0.1 V and the second vertex at −1.0 V, at variable scan rate ranging from 5 mV/s to 200 mV/s.

Ligands (L^{CPn}, no3py, 0.1 mM) and their Cu(II)-complexes (0.1 mM) were analysed in 0.1 M sodium acetate solution. $Cu(CH_3COO)_2$ was used as a source for Cu^{2+}.

3. Results and discussion

3.1. Design of the MCT1 targeting bioconjugate

The design of the bioconjugate involves the strategic selection of its three main fragments: *i)* the targeting molecule, *ii)* the bifunctional chelator (BFC), and *iii)* the spacer/linker. The targeting molecule is proposed herein on the basis of docking studies, starting form the lead compound 7ACC2. Wang et al. reported the crystal structure of MCT1 co-crystalized either with its natural ligand lactate as well as with three inhibitors, namely AZD3965, BAY-8002, and 7ACC2 [13]. MCT1 has two possible conformations: the "outward-open", in which the interaction occurs when the protein cavity is accessible from the extracellular side of the membrane, and the "inward-open" where the cavity is

accessible from the cytoplasmatic side of the cellular membrane (Fig. S2). Interestingly, lactate, BAY-8002 and AZD3965 binds the "outward open" conformer, while 7ACC2 blocks the protein in the "inward open" conformation [13].

As shown in Fig. 3, the coumarin moiety of 7ACC2 (blue scaffold) was selected as the starting point to design compound **1** (3-carboxy,7 hydroxy-coumarin) and investigated as targeting molecule. A reactive phenolic group, aimed at further coupling with the spacer and chelator, was introduced in position 7 in place of the nitrogen atom of 7ACC2. Crystal data were exploited to perform computational docking studies and pose comparison of the two compounds to predict the potential affinity of **1** for MCT1. The "inward-open" conformation of MCT1 was selected for analysis, consistently with crystallographic data [13].

Docking experiments suggest that the presence of a carboxylic group at position 2 is crucial for inhibitory activity and for structural similarity to lactate [44]. Besides, coumarin analogue **1** (Fig. 4) recapitulates the binding mode of 7ACC2, with the coumarin ring occupying the central pocket of the lactate binding site formed by **Tyr34**, **Leu66**, **Phe278**, **Leu281**, **Val282**, and **Phe367**, and the carboxylate group interacting with **Lys38**, **Ser154**, **Asp309** (Fig. 4).

The analysis of Slc16A1/MCT1 expression levels, using data from the TCGA and GTEx databases, reveals a significant increase in its transcriptional levels in prostate tissues of cancer patients relative to healthy individuals (Fig. S3A). Consequently, we examined if the expression of MCT1 is altered in neoplastic epithelial prostate cells in comparison to normal ones. qRT-PCR analysis across various prostate cell lines (Fig. S3B) demonstrated that healthy cells (RWPE1 and PrEC) exhibit markedly lower levels of Slc16A1/MCT1 compared to both androgen-unresponsive (PC3 and DU145) and androgen-responsive (LNCaP) cancer cells originating from diverse metastatic sites of prostate cancer. Western Blot analysis of MCT1 protein levels confirmed that PCa cell lines (PC3 and LNCaP) are characterized by higher MCT1 levels compared to RWPE1 basal epithelial cells (Fig. S3C).

In order to verify the interaction of the proposed targeting molecule **1** with MCT1, in vitro biological assays were then carried out in LNCaP cells, which exhibit higher expression of MCT1. Compound **1** was administered to LNCaP cells grown in complete medium and in medium devoid of glucose and glutamine, containing only lactate as an energy source for cellular metabolism (lactate-only medium). Under these two conditions, the analysis of the effect on cell viability enabled us to indirectly ascertain whether compound **1** could have a specific effect on the MCT1 transporter. In fact, the survival of LNCaP cells in lactate-only medium relies on their capacity to import lactate from the extracellular environment via MCT1-mediated uptake. As shown in Fig. 5A, the viability of LNCaP cells was not significantly affected by the administration of compound **1** for 72 h in a glucose-rich environment (complete medium). Conversely, even though the absence of glucose and glutamine in the presence of lactate already leads to reduced cell proliferation, treatment with compound **1** further reduced cell viability by approximately 25 % (from 59.4 % to 43.1 %). These results indicate that compound **1** can, at least partially, suppress MCT1-mediated intake of lactate, which is required for cellular metabolism under this condition. Due to the absence of activity in complete medium, we can rule out the

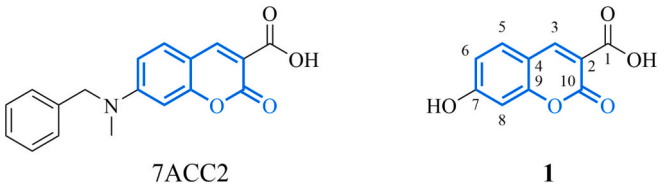

Fig. 3. Chemical structures of the lead molecule 7ACC2 and the targeting compound (**1**) based on coumarin moiety (highlighted in blue). (For interpretation of the references to colour in this figure legend, the reader is referred to the web version of this article.)

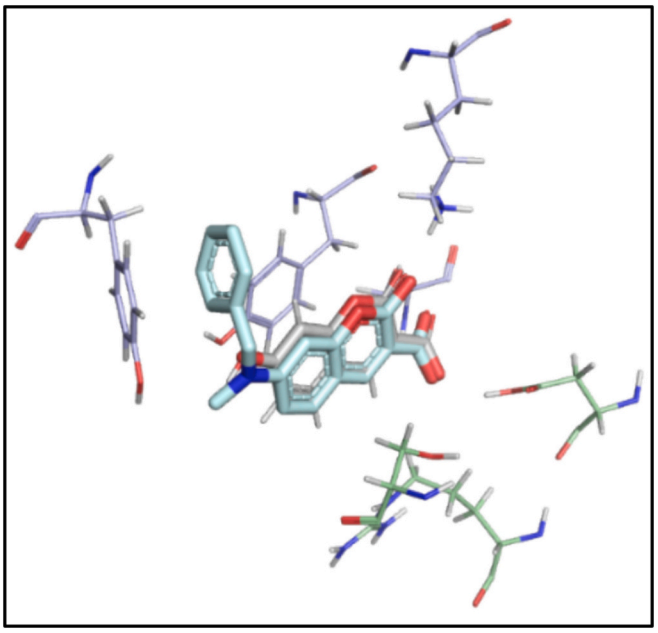

Fig. 4. Calculated binding mode of compound **1** in MCT1 cavity, superimposed with the co-crystallized ligand 7ACC2 (light blue, PDB 7CKO). (For interpretation of the references to colour in this figure legend, the reader is referred to the web version of this article.)

possibility that compound **1** could have a non-specific anti-proliferative effect in LNCaP cells. The inhibitory activity of compound 1 against MCT1 was further determined by applying a functional 3-bromopyruvate (3BP) cell viability assay. In fact, MCT1 is responsible for the bidirectional transport of lactate and pyruvate, and it also facilitates the uptake of 3BP into cancer cells. This uptake is crucial for the cytotoxic effect exerted by 3BP. Exposure of LNCaP cells to 3BP 50 μM for 16 h determined a reduction of cell viability to about 48 % (Fig. 5B). We then performed a pre-treatment of LNCaP cells for 6 h with compound 1 (30 μM) or with the reference MCT1 inhibitor 7ACC2, followed by co-administration with 3BP for 16 h. Under this experimental condition, functional inhibition of MCT1 will result in reduced intracellular 3BP levels and enhanced cell viability compared to 3BP alone. As shown in Fig. 5B, both **1** and 7ACC2 displayed a significant increase in cell proliferation at micromolar concentration ranges, with 7ACC2 50 μM almost completely protecting LNCaP cells from 3BP toxicity. Similar results were also obtained on PC3 tumor cells (Fig. S3, D). These results further indicate that compound **1** can effectively target MCT1 activity.

Having identified the coumarin moiety (**1**) as a promising targeting vector, the selection of the chelator represents the further step. Among the plethora of Cu(II)-chelators, no3py demonstrated the ability to form thermodynamically stable and inert complexes. The bifunctional no3py (no3pyCOOK [45], Fig. 6) is featured with a carboxylic group that can easily react thanks to coupling agents (HBTU, DCC, or HATU) with amines to form the amide linkage under mild conditions with satisfactory yields and short reaction times. The formation of an amide linking group is a well-established method for coupling bifunctional chelators (BFCs) to targeting molecules in view of its biocompatibility, and high stability under physiological conditions [23,46].

As indicated by modelling, a direct linkage of compound **1** to no3pyCOOK does not allow a good fitting of coumarin moiety into MCT1 cavity due to the bulky chelator. In addition to steric hindrance, the positively charged Cu(II)-complex located in proximity of the targeting vector (coumarin) may also hamper the interaction with the hydrophobic pocket of MCT1, as predicted from docking calculations. To address this issue, a suitable spacer, such as poly(ethylene glycol) (PEG), has to be added in between the BFC and coumarin moiety. PEG is

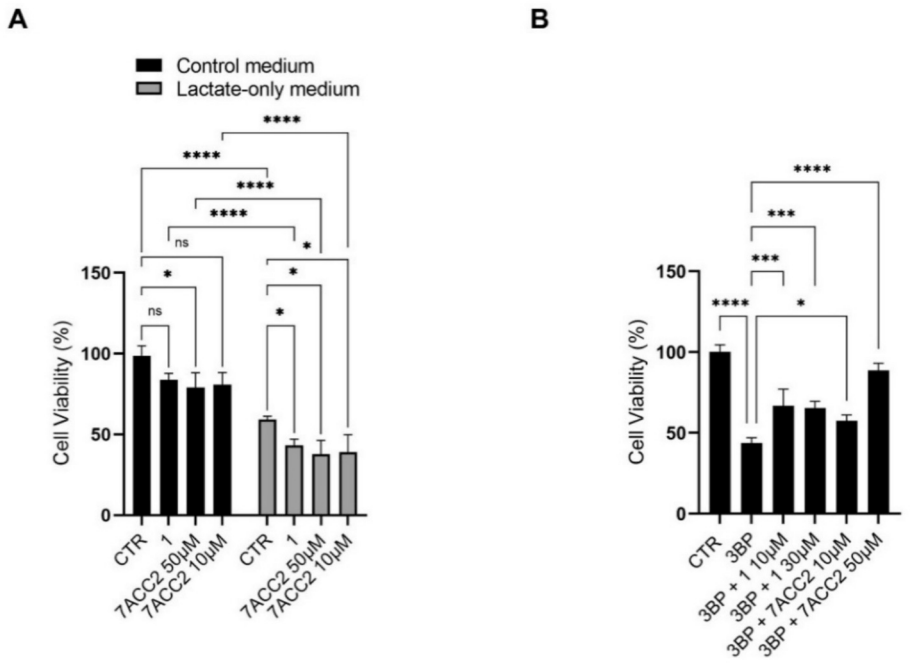

Fig. 5. **A**) Cell viability of LNCaP cells evaluated after 72 h of culture in complete control medium or in medium devoid of Glucose and Glutamine, where lactate is the only fuel for cell metabolism, analysed by PrestoBlue. Data represent mean ± SEM. Cell proliferation of LNCaP cells grown in control medium was arbitrarily set at 100 %. (two-way ANOVA: *$p < 0.05$, ***$p < 0.001$, ****$p < 0.0001$, ns = not significant). **B**) A functional 3-bromopyruvate (3BP) cell viability assay was used to assess the MCT1-inhibitory activity of compound **1**, compared to the reference inhibitor 7ACC2. Cell proliferation of LNCaP cells grown in control medium was arbitrarily set at 100 % (one-way ANOVA: *p < 0.05, ***p < 0.001, ****p < 0.0001).

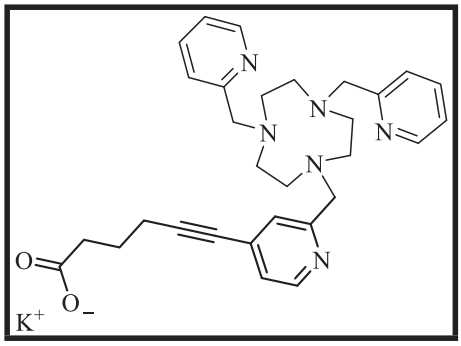

Fig. 6. Chemical structure of the bifunctional chelator (BCF) no3pyCOOK.

largely exploited to improve the hydrophilicity, regulate nonspecific clearance mechanisms, and optimize circulation time in vivo, aspects of major importance in radiopharmaceuticals [47–52]. As shown in Fig. 7, modelling suggested a possible length for the PEG chain (> 34.3 Å) to reduce its interaction with the biological target and keep the chelator outside the intracellular environment. The optimal estimated distance is consistent with a PEG_3 moiety (37.3 Å) that ensures the fitting of coumarin portion with the hydrophobic membrane transporter protein while keeping the hydrophilic portion (copper complex) external.

3.2. Synthesis

The targeting moiety (**1**) was prepared in two steps, starting from the Knoevenagel condensation of a substituted 2-hydroxo benzaldehyde and diethyl malonate that allowed the formation of the ester derivative **2.** The reaction conditions reported by Xiao et al. [53] were improved by using sonication that reduced the reaction time from 16 h to 1 h. More importantly, pure compound **2** is obtained through recrystallization from ethanol. The second step, leading from compound **2** to **1**, consists

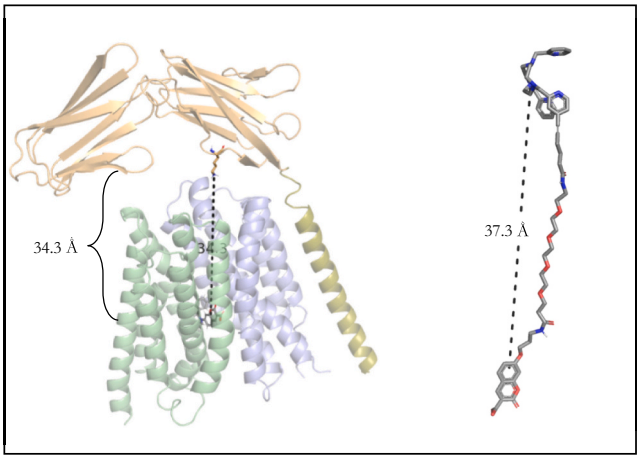

Fig. 7. Evaluation of the optimal linker length for the bioconjugate (**C**oumarin-**PEG**$_3$-**n**o3py, $\mathbf{L^{CPn}}$): the distance between the binding pocket and the extracellular space (left) is consistent with a PEG_3 linker (right).

in a simple ester hydrolysis in alkaline medium.

The synthesis of the bioconjugate $\mathbf{L^{CPn}}$ requires the PEGylation of the targeting moiety (**1**) (Scheme 1) followed by its coupling with no3py-COOK (Scheme 2) achieved by HBTU activation (Scheme 3).

The addition of the PEG_3 spacer to the coumarin moiety is a two-step process that comprises a first nucleophilic substitution (SN_2) of the phenolic oxygen with N-Boc propyl bromide and the coupling reaction with a PEG derivative catalyzed by HBTU and DIPEA (Scheme 1). After Boc removal, PEGylated coumarin (**6**) is quantitatively isolated.

Despite very good yields and easy work-up, the synthesis of no2py (**10**) reported in the literature requires up to 13 days to be completed, particularly long is the second step that takes 1 week (Scheme S1) [54,55]. An alternative synthetic route has been explored which allows

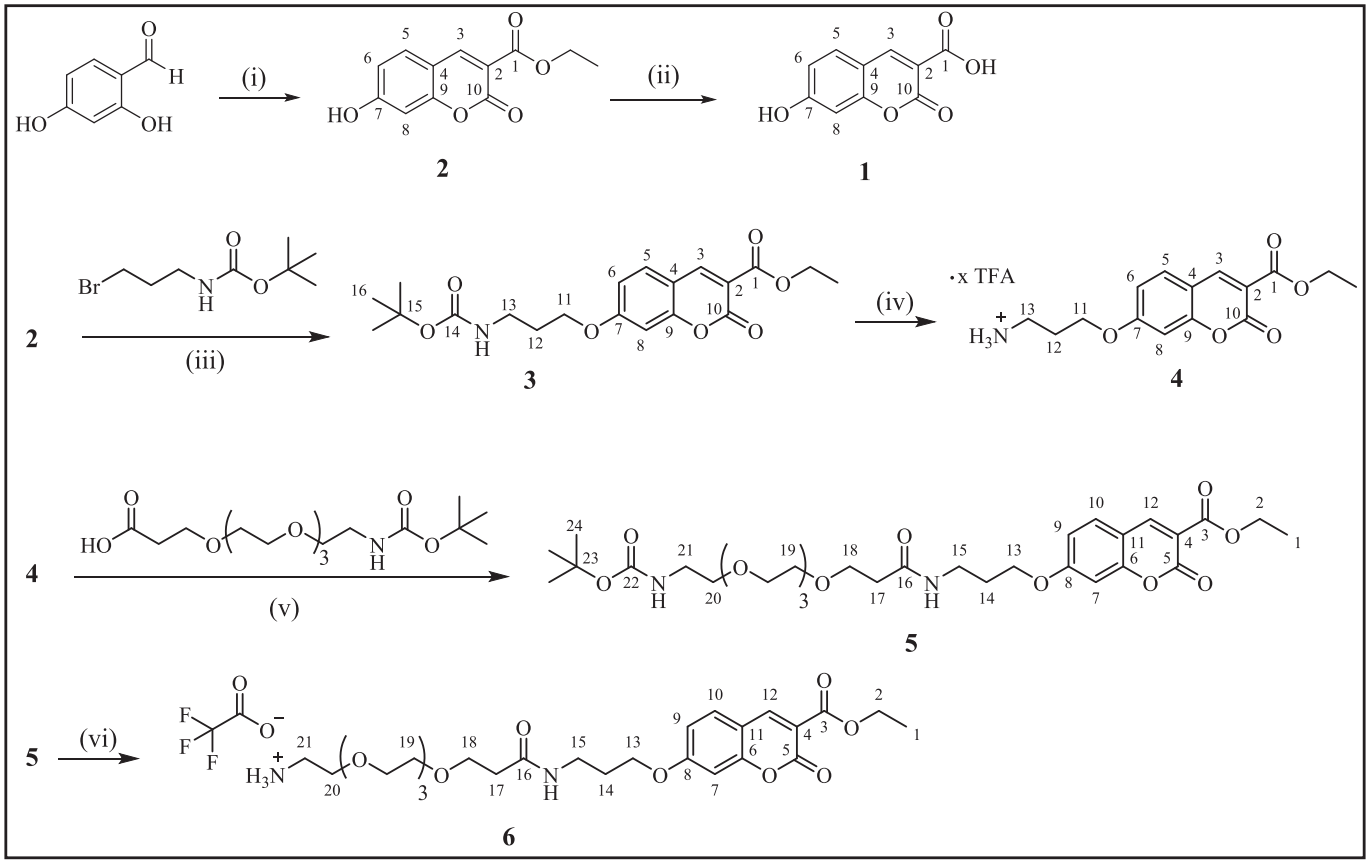

Scheme 1. Synthesis of PEGylated coumarin (**6**): (i) diethyl malonate, piperidine, sonicated 2 h; (ii) LiOH (2 M solution), MeOH, 4 h; (iii) Cs_2CO_3, KI, DMF, 70 °C overnight; (iv) TFA, DCM, RT, 2 h; (v) HBTU, DIPEA, DMF, 50 °C, overnight; (vi) TFA, DCM, RT, 2 h.

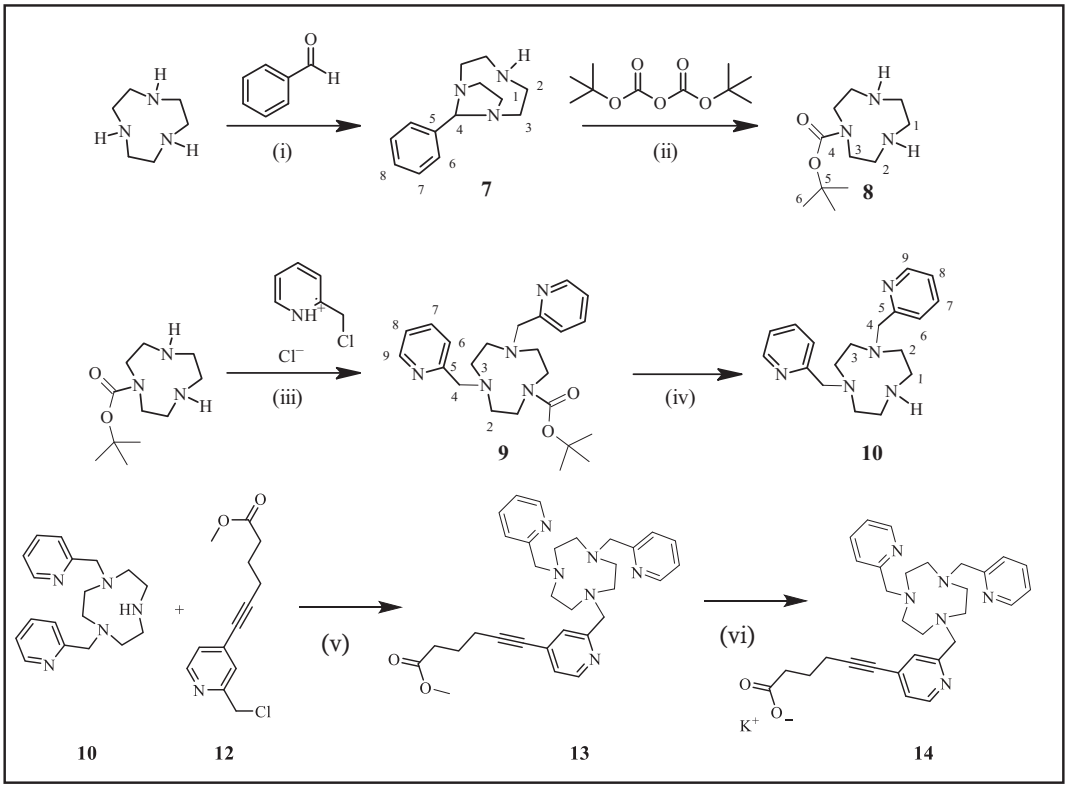

Scheme 2. Newly designed synthesis of compound **10** (no2py) and bifunctional chelator no3pyCOOK (**14**): (i) EtOH, RT, overnight; (ii) TEA, DCM, RT, 6 h; (iii) K_2CO_3, dry ACN, RT, 3 days; (iv) TFA, DCM, RT, 1 h. (v) K_2CO_3, dry ACN, RT, 3 days; (vi) KOH 1 M, THF, 50 °C, overnight.

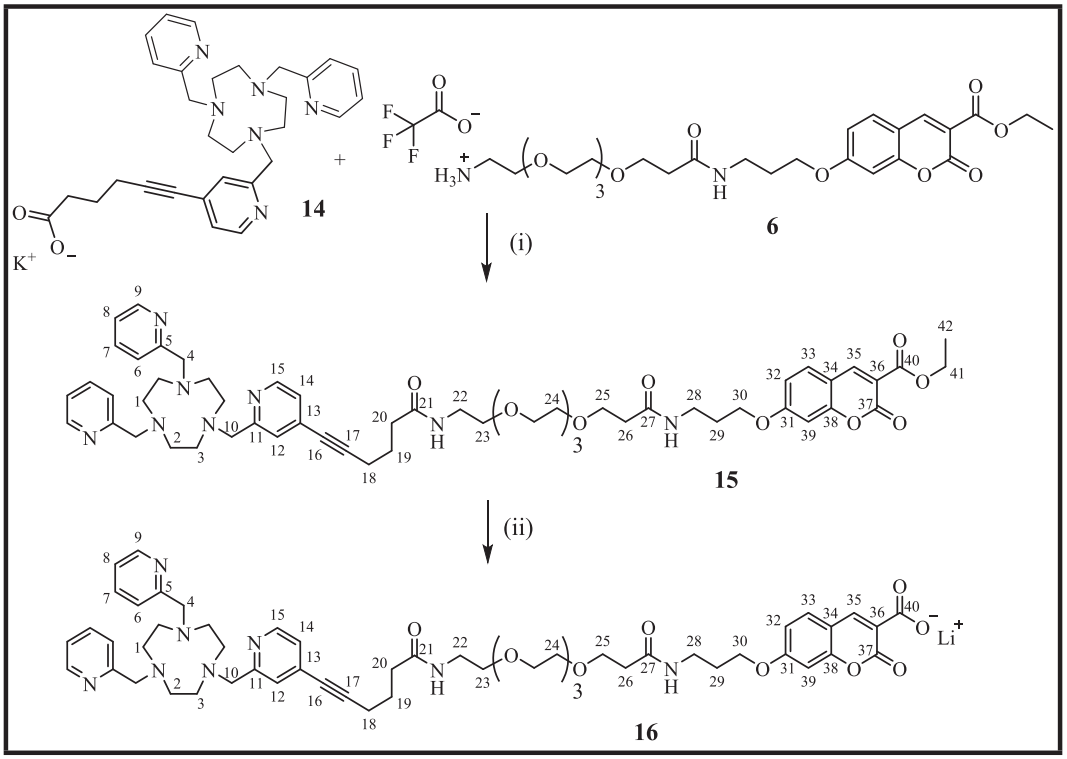

Scheme 3. Synthesis of $\mathbf{L}^{\mathbf{CPn}}$ bioconjugate (**16**): (i) HBTU, DIPEA, DMF, 50 °C, overnight; (ii) LiOH, MeOH, RT, 30 min.

to obtain intermediates **8** and **10** useful for the synthesis of asymmetric TACN derivatives (Scheme 2). The key reaction is the protection of two amines of TACN as aminal (**7**) and the following Boc protection. During the alumina column chromatography to purify the aminal Boc-protected compound (**8i**), the labile aminal group was cleaved, giving directly the mono-Boc protected TACN (**8**) in one step. Two pyridine arms were added to form compound **9** that was purified by flash alumina column chromatography. The final deprotection step requires only sonication for one hour with trifluoracetic acid (TFA). Compound **10** was isolated in pure form through alkaline extraction. The overall yield (44 %) is comparable to the results reported by Roger et al. [54].

Differently from the previously reported study [56], the synthesis of no3pyCOOK was carried out through the alkyl chloride intermediate (**12**) instead of the corresponding mesylated compound, resulting in a reduction of side reactions due to extremely high reactivity of mesylate leaving group.

The overall synthesis of no3pyCOOK (**14**) proved to be more efficient compared to the one previously reported with the mesylated compound, especially in terms of yield (66 % vs. 52 %). Two main factors contribute to this achievement: *i)* the lower reactivity of the alkyl chloride compared to the mesyl group reduces the formation of side quaternarization products; *ii)* the column chromatography used to purify the intermediate **13** was performed using de-activated alumina (grade III instead of grade I). This is meant to decrease the aggressiveness of alumina, which should lead to reduce hydrolysis of the methyl ester. In addition, unreacted compound **12** can be totally recovered during the column chromatography and recycled. Finally, the bioconjugate $\mathbf{L}^{\mathbf{CPn}}$ (**16**) is obtained by the coupling reaction between **6** and **14** according to Scheme 3.

3.3. Acid/base properties

$\mathbf{L}^{\mathbf{CPn}}$ (**16**) is a polyprotic weak acid characterized by a carboxylic group on the coumarin moiety, three aliphatic tertiary amines of TACN and three pyridine groups. In its neutral form, the bioconjugate can be represented as HL^{CPn} (referred to as HL in equilibrium reactions). Investigating the acid-base behaviour is of pillar importance to predict speciation as function of pH and consequently forecast metal complexation. ^{1}H NMR and UV–vis spectroscopies were applied to determine the proton dissociation constants (pK_a) of $\mathbf{L}^{\mathbf{CPn}}$.

^{1}H NMR spectra of $\mathbf{L}^{\mathbf{CPn}}$ at different pH are reported in Fig. 8. The coumarin portion is characterized by four signals in the aromatic region (8.2–6.7 ppm), and three signals belonging to the propyl chain that appear in the aliphatic region (4.3–1.9 ppm). no3py shows signals both in the aromatic region due to pyridine rings (8.7–7.1 ppm), and in the aliphatic one due to ethylene moieties of the macrocycle and methylene groups of the picolyl arms (4.3–1.7 ppm). PEG signals are observed at 3.6 ppm.

Spectral changes were investigated in the pH range 0.6–10.6; above this upper limit a precipitate formed preventing the titration at higher pH. As the pH increases, almost all signals undergo upfield shifts due to deprotonation hence intensification in electronic density (Fig. 8 and S4). Pyridine protons (H-9, H-12 and H-15) behave differently; indeed, they shift up-field until reaching a minimum value of chemical shift at pH 5 while they move downfield increasing the pH. This behaviour could be explained by the deprotonation of pyridinium below pH 5, followed by the involvement of pyridine nitrogen in an intramolecular H-bond with the protonated ring amine. TACN methylene protons are extremely broad (3.0–3.3 ppm, pH 0.65) and change their spectral patterns during the titration, particularly they collapse until pH ~3 to separate again as pH increases, suggesting that proton dissociation occurs between pH 5 and 10. The singlet H-35 in *ortho* position to the carboxylic group clearly highlights a proton dissociation at pH ~4.

Due to solubility limits in basic conditions (pH >10), ^{1}H NMR data were complemented with pH-dependent UV–vis titrations, as reported in Fig. 9.

The UV–vis spectra partly resemble the pH-dependent titration of compound **1** (Fig. S5). In particular, at acidic pH both compounds – **1** and L^{CPn} - show a maximum at ~360 nm due to electronic transitions of coumarin moiety, the presence of the chromophore phenolic group, present solely in compound **1**, shifts the maximum for this molecule to 390 nm when phenolate is formed (pH > 8). In acidic conditions (pH 2),

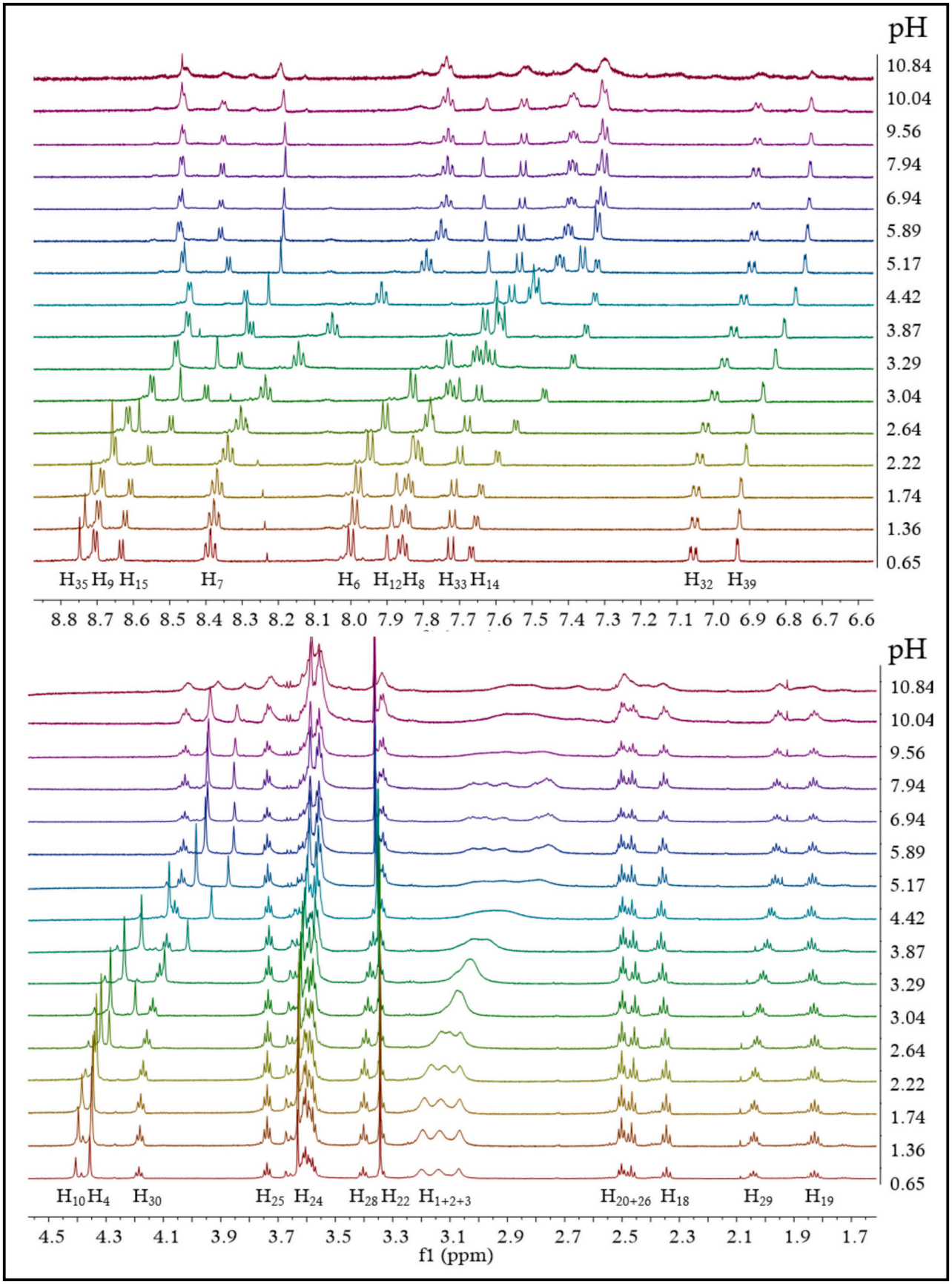

Fig. 8. ^{1}H NMR spectra of $\mathbf{L^{CPn}}$ at different pH values and signal attributions (600 MHz, D_2O, $T = 25$ °C, $I = 0.10$ M NaCl, $[L^{CPn}] = 4$ mM).

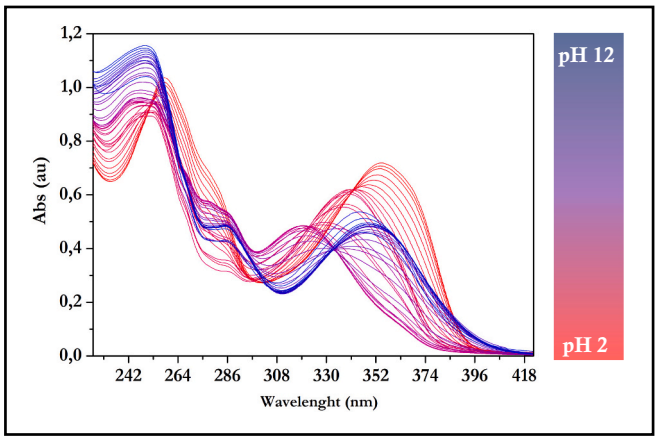

Fig. 9. Representative UV–vis spectra of $\mathbf{L^{CPn}}$ at different pH ([L^{CPn}] = 100 μM, I = 0.1 M NaCl, T = 25 °C).

in addition to the absorption at 360 nm, the ligand L^{CPn} shows a maximum at 260 nm with a shoulder at 280 nm. As long as the pH is increased to pH 5 an hypsochromic shift is observed for both maxima and an isosbestic point appears at 340 nm. A further hypsochromic shift is observed from 340 nm to 320 nm when pH 7.5 is reached. Finally, in extremely basic conditions (pH > 10) a bathochromic shift is observed for the maximum at 320 nm that reaches a λ_{max} value of 355 nm, another isosbestic point is observed. These results point out the simultaneous coexistence of several solution equilibria.

The pH-dependent changes in the electronic spectra allowed the determination of the acidity constants (pK_a) of L^{CPn}, which are summarized in Table 1. Despite the similarity of the chelator moiety (no3py), the presence of an additional weak acid site (COOH) on coumarin moiety may affect the proton dissociation profiles, impacting on the values of equilibrium constants, as shown in Table 1. The calculated protonation constants are highly sensitive to the analytical technique employed - such as UV–vis spectroscopy, NMR, potentiometry, or calorimetry - as well as to the experimental conditions, particularly the ionic strength. Accordingly, the UV–vis pH-metric titration of the lead chelator no3py was conducted under the same conditions as those used for $\mathbf{L^{CPn}}$. The corresponding results are presented in Table 1 and Figs. S6 and S7. In comparison to no3py and TACN, the higher value of $pK_{a,4}$, possibly attributed to macrocycle ammonium, could be related to an increased basicity due to the presence of the carboxylic moiety and the steric hindrance of the PEG spacer. $pK_{a,3}$ and $pK_{a,2}$ may be assigned to pyridinium dissociations consistently with previously reported data [36,57] and ^{1}H NMR titration. Finally, $pK_{a,1}$ value is consistent with the dissociation of the carboxylic moiety of the coumarin scaffold as supported by the value obtained for compound **1**. It was not possible to detect the last protonation of the macrocycle ring (<2), as commonly observed for analogue azamacrocycles [30,33,58,59].

Based on the pK_a values, the species distribution curves of $\mathbf{L^{CPn}}$ were calculated (Fig. 10). The prevailing species at physiological pH (7.4) is H_2L^+, species in which both pyridine and carboxylic groups are dissociated while two TACN amines are still protonated (ammonium form).

Table 1
Acidity constants (pK_a) of $\mathbf{L^{CPn}}$ and compound **1** (T = 25 °C, I = 0.1 M NaCl) in comparison with analogue chelators. L^- represents the completely deprotonated form of the ligand. The reported uncertainty values were obtained by the fitting procedure and represents one standard deviation unit.

Equilibrium Reaction*		L^{CPn}	no3py[a]	no3py[b]	TACN[c]	1
$HL \rightleftharpoons H^+ + L^-$	$pK_{a,5}$	11.67 ± 0.06	11.07	11.25 ± 0.15	10.68	
$H_2L^+ \rightleftharpoons H^+ + HL$	$pK_{a,4}$	9.34 ± 0.09	5.07	4.77 ± 0.08	6.86	
$H_3L^{2+} \rightleftharpoons H^+ + H_2L^+$	$pK_{a,3}$	6.04 ± 0.06	3.55	3.50 ± 0.08	2.1	
$H_4L^{3+} \rightleftharpoons H^+ + H_3L^{2+}$	$pK_{a,2}$	4.52 ± 0.20	1.78	<2		7.62 ± 0.03
$H_5L^{4+} \rightleftharpoons H^+ + H_4L^{3+}$	$pK_{a,1}$	3.24 ± 0.19	–	–		3.67 ± 0.02

* Equilibrium reactions refers to L^{CPn}.
[a] Taken from ref. [36].
[b] This work (T = 25 °C, I = 0.1 M NaCl).
[c] Taken from ref. [57].

3.4. Metal complexation with copper and zinc

The Cu^{2+} complex of $\mathbf{L^{CPn}}$ was synthesized in situ and its formation was confirmed by High Resolution Mass Spectrometry (Fig. S8). HR-MS data confirmed the 1:1 metal-to-ligand molar ratio, suggesting the binding of Cu^{2+} ion through the no3py chelator (Fig. S9).

UV–vis spectroscopy can be used to investigate the metal complexation, indeed when Cu^{2+} is added to $\mathbf{L^{CPn}}$ solution the formation of a *d-d* transition band is observed with a maximum wavelength around 680 nm depending on the pH (Fig. S10), consistently with the observation previously reported for $[Cu(no3py)]^{2+}$ that displays an absorption at 688 nm in 0.1 M sodium acetate [36]. When the pH is increased from 2 to 10, a slight hypsochromic shift of the maximum wavelength is observed from 693 nm to 669 nm, tentatively attributed to the formation of a mixed hydroxo-complex.

The pH-dependent UV–vis titration of the Cu(II)-L^{CPn} 1:1 system (Fig. 11A) allowed to estimate the overall stability constants of three complex species: $[CuHL^{CPn}]^{2+}$ ($\log\beta_{111}$ = 27.50 ± 0.01), $[CuL^{CPn}]^+$ ($\log\beta_{110}$ = 24.09 ± 0.02) and $[CuL^{CPn}(OH)]$ ($\log\beta_{11-1}$ = 16.70 ± 0.04). Stepwise stability constant (logK) together with pCu^{2+} values are reported in Table 2 in comparison to no3py system. In acid conditions (pH ~4) the species distribution plot (Fig. 11B) highlights the presence of the species $[CuHL]^{2+}$, which is attributed to the protonation of the carboxylate moiety of L^{CPn}. At physiological pH (7.4), the major species are $[CuL^{CPn}]^+$ and $[CuL^{CPn}(OH)]$, with the latter becoming dominant in basic conditions (pH > 9). The incorporation of the spacer/linker into the no3py moiety appears to modulate the overall stability constant of the ML species, resulting in a decrease compared to the parent no3py chelator (27.4 [36]). Nevertheless, the complex remains more stable than the picolinate-based derivative H_3no3pa (16.21 [36]). As illustrated in Table 2, a more informative comparison of chelator efficacy is provided by the pCu^{2+} values: although $\mathbf{L^{CPn}}$ is surpassed by no3py

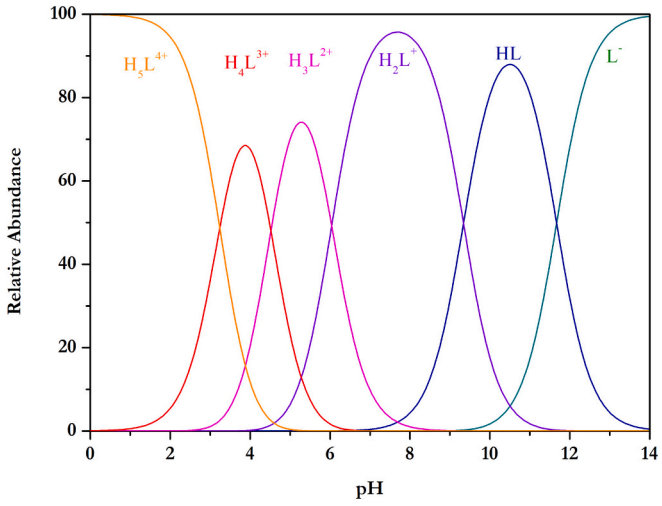

Fig. 10. Species distribution diagram for $\mathbf{L^{CPn}}$ (0.1 mM), data were calculated from overall protonation constants ($\log\beta_{HL}$) using PyES [60].

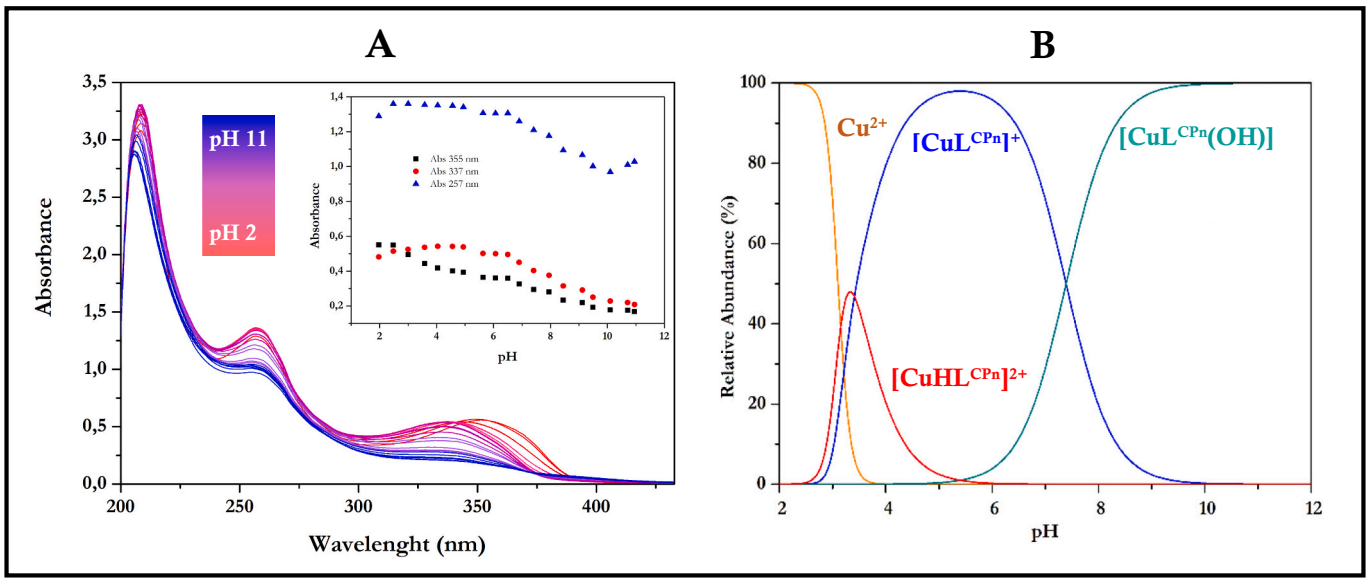

Fig. 11. **A**) pH-dependent UV–vis titration of Cu^{2+}-L^{CPn} system ($C_{Cu} = C_L = 100$ μM, $I = 0.1$ M NaCl, 25 °C); **B**) plot of species distribution curves ($C_L = 10C_{Cu} = 10$ μM) calculated using PyES [60].

Table 2
Equilibrium reactions, logarithm of stepwise stability constants (logK) and pCu^{2+} ($-\log[Cu^{2+}_{free}]$, calculated at pH 7.4, $C_L = 10C_{Cu} = 10$ μM) for Cu^{2+} systems. The reported uncertainty values were obtained by the fitting procedure and represents one standard deviation unit.

Equilibrium reaction[a]	logK	L^{CPn}[b]	no3py [c]
$Cu^{2+} + L \rightleftharpoons CuL$	$\log\beta_{110}$	24.09 ± 0.02	27.4
$CuL + H^+ \rightleftharpoons CuHL$	$\log\beta_{111}$ - $\log\beta_{110}$	3.41 ± 0.03	2.13
$CuL(OH) + H^+ \rightleftharpoons CuL$	$\log\beta_{110}$ - $\log\beta_{11-1}$	7.39 ± 0.06	11.65
	pCu^{2+}	**19.2**	**24.7**

[a] The charges of the ligand and complex species are omitted for clarity.
[b] This work, $T = 25$ °C, $I = 0.1$ M NaCl.
[c] Taken from ref. [36].

(19.2 vs. 27.4), it demonstrates superior efficiency compared to the widely used chelators NOTA (18.2) and DOTA (17.4) under identical conditions [32].

In order to complete the structural study in solution, Zn^{2+} was used as an NMR probe of Cu^{2+}. These two metal ions exhibit significant similarities in their coordination chemistry, including their coordination modes and ligand preferences for oxygenated and nitrogenated ligands and allow for complementary methods of detection [61]. HR-MS confirmed for the Zn^{2+} system the formation of the same complex species observed in presence of Cu^{2+} (Figs. S11 and 12).

Upon Zn^{2+} coordination, several changes in the ^{1}H NMR spectrum of **L^{CPn}** are detectable (Fig. 12). The majority of the signals are down-field shifted as a consequence of the increase in the positive charge. As an exception, the aromatic protons in *ortho*-position to the pyridinic nitrogen are upfield-shifted. This is a common behaviour displayed also by other no3py derivatives [62] and confirms the coordination of Zn^{2+}.

The slight shifts observed for the coumarin protons upon Zn^{2+} addition may suggest an interaction of the carboxylate group with the metal ion and a weak competition with the no3py moiety for metal binding. This behaviour might account, together with the steric hindrance of the PEG_3 chain, for the lower thermodynamic stability of $[CuL^{CPn}]^+$ with respect to $[Cu(no3py)]^{2+}$.

3.5. Cellular uptake

To validate the potential interaction between the bioconjugate $[CuL^{CPn}]^+$ and the MCT1 transporter, we quantified the intracellular copper complex. Due to the unexpectedly low fluorescence emission of $[CuL^{CPn}]^+$ (Fig. S13) compared to coumarin, fluorescence-based techniques were not feasible. Therefore, we employed inductively coupled plasma mass spectrometry (ICP-MS) to estimate the amount of the internalized complex. We first assessed the toxicity of the copper complex on both healthy (RWPE1) and tumor (LNCaP and PC3) cells treated for 24 h with $[CuL^{CPn}]^+$ (50 μM), finding a slight reduction in cell viability only in LNCaP cells (Fig. 13A). We then quantified the complex's uptake in RWPE1 and PC3 cells to account for lines with different levels of MCT1 expression and to minimize potential indirect variances due to changes in cell viability. As shown in Fig. 13B, a modest but selective increase in copper uptake was observed in PC3 cells, consistent with the overexpression of MCT1 in this cell line compared with healthy RWPE1 cells. Although the absolute amount of internalized copper is relatively low, the data support the hypothesis that the bioconjugate interacts with the MCT1 binding pocket via the coumarin moiety, while the Cu-no3py complex likely remains at the cell membrane surface, as suggested by molecular docking studies. It is also plausible that partial removal of the membrane-bound bioconjugate occurred during the washing steps, contributing to the low observed uptake levels.

3.6. Cu^{2+}/Cu^+ redox cycling: a mandatory parameter for in vivo applications

The endogenous reduction window refers to the range of redox potentials within which biological reduction processes can occur in vivo. It is defined by the reducing and oxidizing agents naturally present in living systems. The estimated potential threshold for common bioreductants is approximately −0.64 V vs. SCE, which correspond to −0.400 V vs NHE and − 0.605 V vs Ag/AgCl (3 M) [42]. Cyclic voltammetry (CV) was performed on **L^{CPn}**, its Cu (II) complex and for comparison on Cu(II)-no3py as reference system to estimate redox potential and assess the ability of the new bioconjugate to stabilize both copper oxidation states. CV were acquired at different scan rates and the plotting of the cathodic and anodic peak current vs. the square root of the scan rate is reported in Fig. S14. The trend for both anodic and cathodic peak current is linear, confirming that electrochemical process is diffusion driven [63].

Fig. 14 show the differences between the redox behaviour of the free ligand L^{CPn} and its Cu^{2+} complex. In the potential range − 1.00 ÷ −0.20

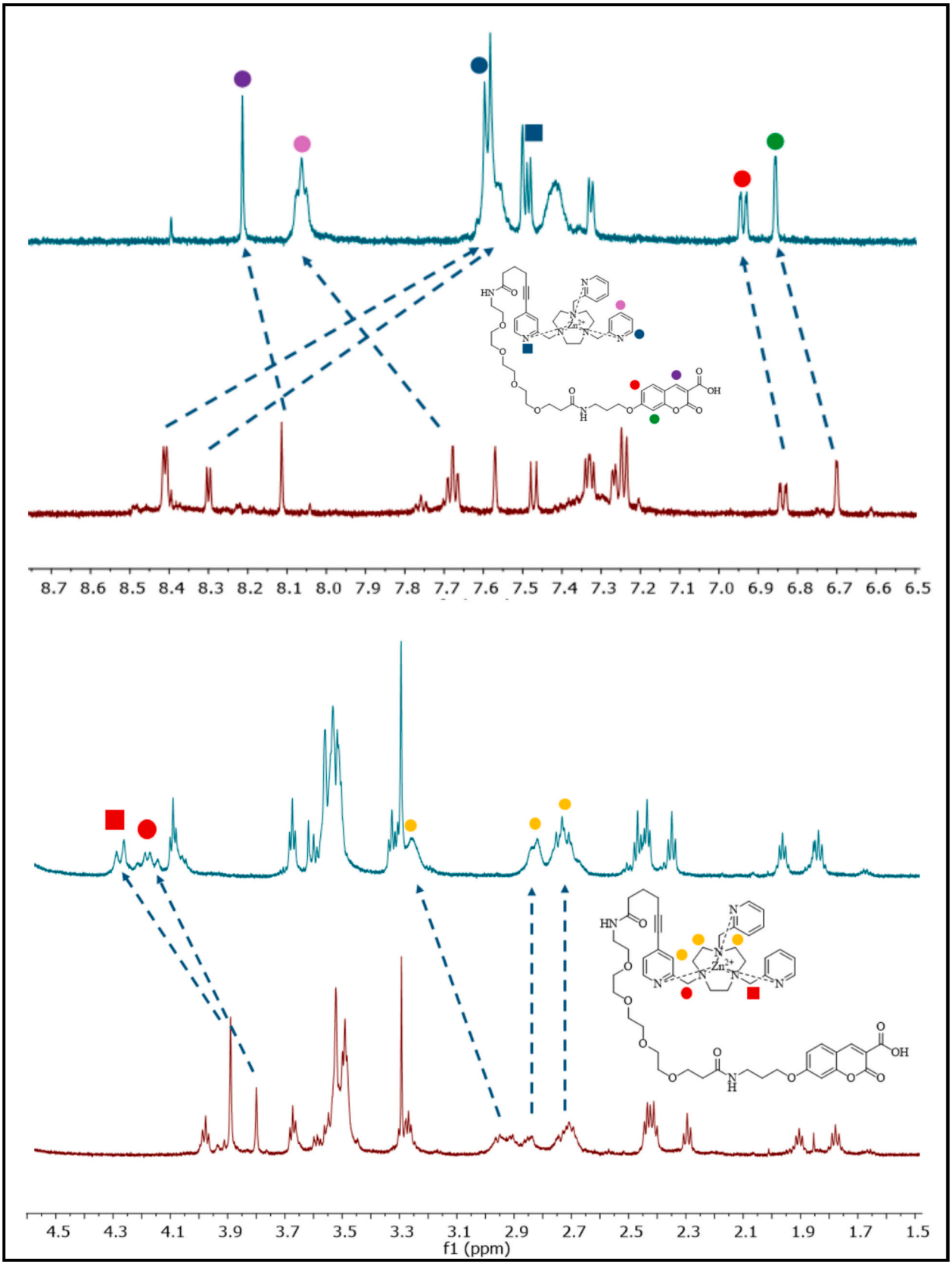

Fig. 12. Comparison between ^{1}H NMR spectra of free ligand $\mathbf{L^{CPn}}$ (bottom, dark red) and Zn^{2+}-L^{CPn} 1:1 system (top, cyan) (600 MHz, D_2O, pH 7, 25 °C). (For interpretation of the references to colour in this figure legend, the reader is referred to the web version of this article.)

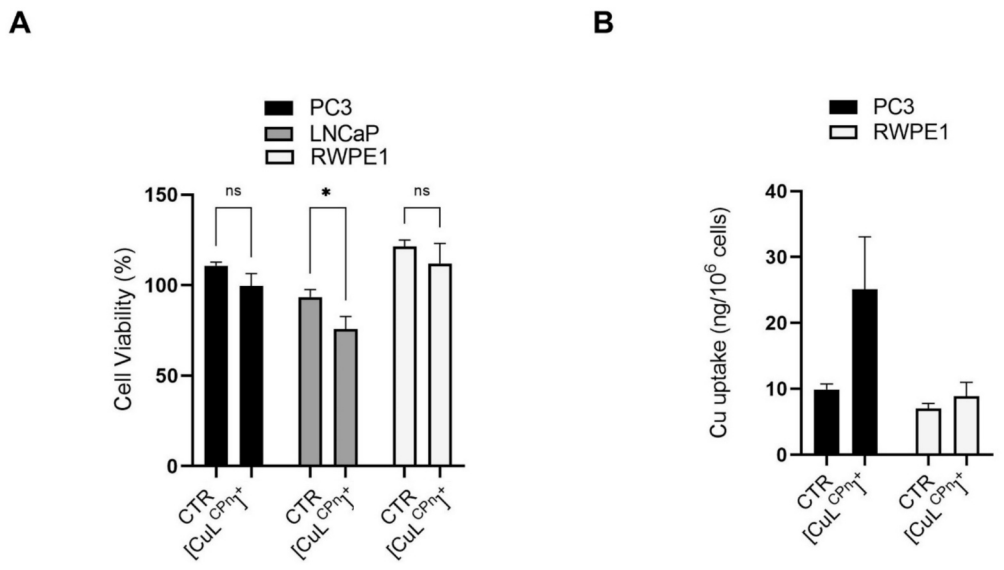

Fig. 13. **A**) Cell viability of PC3, LNCaP and RWPE1 cells after 24 h of treatment with the bioconjugate $[CuL^{CPn}]^+$, analysed by PrestoBlue assay. Data represent mean ± SEM. Cell proliferation of untreated cells (CTR) was arbitrarily set at 100 %. (two-way ANOVA: $^*p < 0.05$, ns = not significant). **B**) Comparison of internalized copper in PC3 (grey) and RWPE1 (black) cells after 24 h incubation with $[CuL^{CPn}]^+$ at the 50 μM dosage in comparison to control. The amount of internalized copper is normalized for a million of treated cells and expressed as ng/10^6 cells. Values are indicated as means ± SEM (vertical bar).

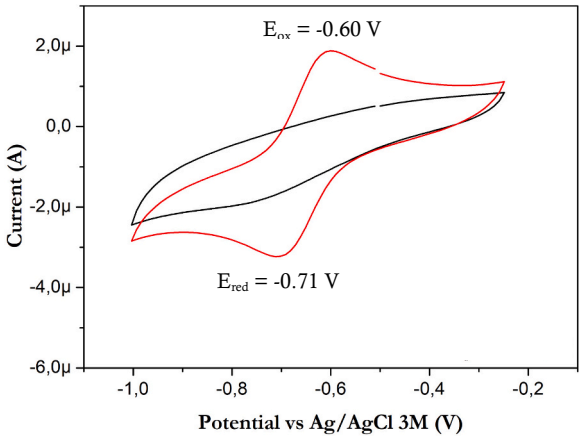

Fig. 14. Cyclic voltammograms of Cu-L^{CPn} system($C_{Cu} = C_{L^{CPn}} = 0.1$ mM; red curve) and L^{CPn} ($C_{L^{CPn}} = 0.1$ mM; black curve) in aqueous solution ($C_{CH_3COONa} = 0.1$ M, $T = 25$ °C, scan rate 50 mV/s). (For interpretation of the references to colour in this figure legend, the reader is referred to the web version of this article.)

V, the ligand itself does not show any evident peak, just a slight broad reduction around −0.80 V. On the other hand, when Cu^{2+} is added, there is an immediate change in the voltammogram: the typical "duck" shape appears with a reduction peak at −0.71 V and the related oxidation peak at −0.60 V, revealing a reversible process. The $E_{1/2}$ values, calculated as $E_{1/2} = (E_{pa} + E_{pc})/2$ for the Cu^{2+} complexes with $\mathbf{L^{CPn}}$ and **no3py**, are reported in Table 3. The $E_{1/2}$ value for Cu^{2+}-L^{CPn} ($E_{1/2} = -656$ mV) is slightly more positive than that of Cu^{2+}-no3py ($E_{1/2} = -696$ mV), which is in good accordance with the literature value ($E_{1/2} = -704$ mV). However, assuming that $E_0 \sim E_{1/2}$ the standard potential of Cu^{2+}-L^{CPn} is lower than the estimated threshold for bioreduction (−605 mV [64]). Therefore, it can reasonably be predicted that in the $[CuL^{CPn}]^+$ complex, copper should remain in its +2 oxidation state under physiological conditions. This behaviour account for avoiding demetallation phenomena caused by the differences in coordination between Cu^{2+} and Cu^+.

Table 3
CV results for Cu^{2+}-L systems (L = L^{CPn}, no3py; $C_{Cu} = C_L = 0.1$ mM, $C_{CH_3COONa} = 0.1$ M, $T = 25$ °C, scan rate 50 mV/s, Ag/AgCl (3 M)).

	L^{CPn}	no3py[a]	no3py[b]
E_{ox} (mV)	−601	−651	−667
E_{red} (mV)	−711	−742	−742
ΔE (mV)	110	91	75
$E_{1/2}$ (mV)	−656	−696	−704

[a] This work.
[b] Taken from ref. [36].

4. Conclusions

The synthesis and full characterization of the chimeric bioconjugate $\mathbf{L^{CPn}}$ was successfully achieved. When compared to some previously reported analogues, key optimizations were introduced, including the mono-Boc protection of the TACN macrocycle and the use of thionyl chloride for more efficient activation in the SN_2-coupling step. The final "bioconjugate" was extensively characterized by 1D and 2D NMR and HRMS experiments, confirming the structure of the expected molecule.

The acid–base behaviour of L^{CPn} was investigated through combined UV–vis and ^{1}H NMR titrations, enabling the assignment of five protonation constants. These values reflect the contribution of both the TACN core and the appended functional groups, and support the structural targeted design. Complex formation with Cu^{2+} and Zn^{2+} was confirmed by several analytical techniques that supported the presence in solution of well-defined 1:1 complex. In particular, the cyclic voltammetry of the copper complex demonstrated a quasi-reversible redox process, with potentials only slightly affected by the conjugation to the coumarin moiety. This suggests that the electronic properties of the no3py moiety are basically preserved and that the complex remains suitable for biological applications, minimizing the risk of Cu^{2+} reduction and in vivo demetallation.

Beyond the physicochemical characterization, docking studies confirmed that L^{CPn} maintains high affinity for the MCT1 transporter. Cellular assays performed under different nutrient availability conditions supported the ability of coumarin moiety (**1**) to inhibit cell proliferation specifically when LNCaP are grown under conditions where lactate-uptake mediated by MCT1 is essential for cell survival and energy metabolism. Moreover, compound **1** was able to partially protect

LNCaP and PC3 cells from cytotoxicity induced by 3BP, which is imported via MCT1. On this basis, it is likely that the molecule will be able to target MCT1 in in vitro cellular models as well, in line with the biological activity of the coumarin-based pharmacophore. Preliminary in vitro investigations advised the interaction of $[CuL^{CPn}]^+$ with the membrane transporter MCT1, as shown by the selective increase of copper uptake in MCT1 overexpressing cell line (PC3) in comparison to basal epithelial RWPE1 cells. These outcomes support the hypothesis that $[CuL^{CPn}]^+$ complex is able to target MCT1 in in vitro cellular models, in line with the biological activity of the coumarin-based pharmacophore.

Altogether, these results support the potential of L^{CPn} as a dual-functional bioconjugate, integrating a robust copper-chelating unit and a selective MCT1-targeting vector. This molecular platform is a promising candidate for future theranostics applications using copper radioisotopes, particularly in cancers with over-expressed MCT1.

CRediT authorship contribution statement

Matteo Mari: Writing – original draft, Investigation, Formal analysis, Data curation. **Silvia Belluti:** Writing – review & editing, Project administration, Investigation, Funding acquisition, Data curation. **Luca Pampanella:** Methodology, Investigation. **Carol Imbriano:** Writing – review & editing, Supervision. **Alfonso Zambon:** Writing – review & editing, Supervision, Software, Data curation. **Jennifer Storchi:** Writing – review & editing. **Laura Pigani:** Writing – review & editing, Methodology, Data curation. **Marianna Tosato:** Writing – review & editing, Funding acquisition. **Sara Rubagotti:** Writing – review & editing. **Pier Cesare Capponi:** Writing – original draft. **Mattia Asti:** Writing – review & editing, Funding acquisition. **Véronique Patinec:** Writing – review & editing, Supervision, Methodology, Data curation. **Raphaël Tripier:** Writing – review & editing, Supervision, Project administration, Funding acquisition, Conceptualization. **Erika Ferrari:** Writing – review & editing, Writing – original draft, Project administration, Investigation, Funding acquisition, Conceptualization.

Declaration of competing interest

The authors declare that they have no known competing financial interests or personal relationships that could have appeared to influence the work reported in this paper.

Acknowledgments

The work was supported by the "FONDO DI ATENEO PER LA RICERCA 2024 - FAR2024 FOMO per progetti di ricerca interdisciplinari" (DR 1307/2024, Prot n. 323715, CUP E53C24003620007). M.M., S.B., L.P. and E.F. thank the Fondazione di Modena (https://www.fondazionedimodena.it) for financially supporting the project. The work was partly supported by the Italian Ministry of Health - Ricerca Corrente Annual Program 2025 (M.A.), AUSL-IRCCS Reggio Emilia (Italy). The authors gratefully acknowledge the Université de Bretagne Occidentale for hosting M.M. during his doctoral mobility, supported by the "Incoming mobility grants for international PhD students in Brittany" program (UBO-DEVE, 2023 – Call 1). We also thank the Erasmus+ programme and the interinstitutional partnership between UNIMORE and UBO for facilitating this international research collaboration. The authors are thankful to the NECTAR Cost Action (CA 18202; https://www.cost-nectar.eu/) for collecting and analyzing equilibrium constants for hydrolysis and associated equilibria in critical compilations. The authors would like to thank the "Centro Interdipartimentale Grandi Strumenti - C.I.G.S." of the University of Modena and Reggio Emilia (https://www.cigs.unimore.it) for NMR, mass spectrometers and their precious technical support.

Appendix A. Supplementary data

Supplementary data to this article can be found online at https://doi.org/10.1016/j.jinorgbio.2025.113130.

References

[1] M.A. Felmlee, R.S. Jones, V. Rodriguez-Cruz, K.E. Follman, M.E. Morris, Monocarboxylate transporters (SLC16): function, regulation, and role in health and disease, Pharmacol. Rev. 72 (2020) 466–485, https://doi.org/10.1124/pr.119.018762.

[2] T. Liu, S. Han, Y. Yao, G. Zhang, Role of human monocarboxylate transporter 1 (hMCT1) and 4 (hMCT4) in tumor cells and the tumor microenvironment, Cancer Manag. Res. 15 (2023) 957–975, https://doi.org/10.2147/CMAR.S421771.

[3] M. Sadeghzadeh, B. Wenzel, D. Gündel, W. Deuther-Conrad, M. Toussaint, R. P. Moldovan, S. Fischer, F.A. Ludwig, R. Teodoro, S. Jonnalagadda, S. K. Jonnalagadda, G. Schüürmann, V.R. Mereddy, L.R. Drewes, P. Brust, Development of novel analogs of the monocarboxylate transporter ligand FACH and biological validation of one potential radiotracer for positron emission tomography (PET) imaging, Molecules 25 (2020), https://doi.org/10.3390/molecules25102309.

[4] P. Sonveaux, F. Végran, T. Schroeder, M.C. Wergin, J. Verrax, Z.N. Rabbani, C.J. De Saedeleer, K.M. Kennedy, C. Diepart, B.F. Jordan, M.J. Kelley, B. Gallez, M.L. Wahl, O. Feron, M.W. Dewhirst, Targeting lactate-fueled respiration selectively kills hypoxic tumor cells in mice, J. Clin. Invest. 118 (2008) 3930–3942, https://doi.org/10.1172/JCI36843.

[5] V.L. Payen, E. Mina, V.F. Van Hée, P.E. Porporato, P. Sonveaux, Monocarboxylate transporters in cancer, Mol. Metab. 33 (2020) 48–66, https://doi.org/10.1016/j.molmet.2019.07.006.

[6] J.Y. Lee, I.K. Lee, W.J. Chang, S.M. Ahn, S.H. Lim, H.S. Kim, K.H. Yoo, K.S. Jung, H. N. Song, J.H. Cho, S.Y. Kim, K.M. Kim, S. Lee, S.T. Kim, S.H. Park, J. Lee, J.O. Park, Y.S. Park, H.Y. Lim, W.K. Kang, MCT4 as a potential therapeutic target for metastatic gastric cancer with peritoneal carcinomatosis, Oncotarget 7 (2016) 43492–43503, https://doi.org/10.18632/oncotarget.9523.

[7] Z. Xu, X. Wang, H. Cheng, J. Li, X. Zhang, X. Wang, The role of MCT1 in tumor progression and targeted therapy: a comprehensive review, Front. Immunol. 16 (2025) 1610466, https://doi.org/10.3389/fimmu.2025.1610466.

[8] V. Miranda-Gonçalves, C.S. Gonçalves, S. Granja, J.V. de Castro, R.M. Reis, B. M. Costa, F. Baltazar, MCT1 is a new prognostic biomarker and its therapeutic inhibition boosts response to temozolomide in human glioblastoma, Cancers (Basel) 13 (2021), https://doi.org/10.3390/CANCERS13143468.

[9] K.G. de la Cruz-López, L.J. Castro-Muñoz, D.O. Reyes-Hernández, A. García-Carrancá, J. Manzo-Merino, Lactate in the regulation of tumor microenvironment and therapeutic approaches, Front. Oncol. 9 (2019), https://doi.org/10.3389/FONC.2019.01143.

[10] L. Zhang, Z.S. Song, Z.S. Wang, Y.L. Guo, C.G. Xu, H. Shen, High expression of SLC16A1 as a biomarker to predict poor prognosis of urological cancers, Front. Oncol. 11 (2021) 706883, https://doi.org/10.3389/fonc.2021.706883.

[11] L. Ippolito, G. Comito, M. Parri, M. Iozzo, A. Duatti, F. Virgilio, N. Lorito, M. Bacci, E. Pardella, G. Sandrini, F. Bianchini, R. Damiano, L. Ferrone, G. la Marca, S. Serni, P. Spatafora, C.V. Catapano, A. Morandi, E. Giannoni, P. Chiarugi, Lactate rewires lipid metabolism and sustains a metabolic-epigenetic axis in prostate cancer, Cancer Res. 82 (2022) 1267–1282, https://doi.org/10.1158/0008-5472.can-21-0914.

[12] T. Koltai, L. Fliegel, Exploring monocarboxylate transporter inhibition for cancer treatment, Explor. Target Antitumor. Ther. 5 (2024) 135–169, https://doi.org/10.37349/etat.2024.00210.

[13] N. Wang, X. Jiang, S. Zhang, A. Zhu, Y. Yuan, H. Xu, J. Lei, C. Yan, Structural basis of human monocarboxylate transporter 1 inhibition by anti-cancer drug candidates, Cell 184 (2021) 370–383.e13, https://doi.org/10.1016/J.CELL.2020.11.043.

[14] M. Singh, J. Afonso, D. Sharma, R. Gupta, V. Kumar, R. Rani, F. Baltazar, V. Kumar, Targeting monocarboxylate transporters (MCTs) in cancer: how close are we to the clinics? Semin. Cancer Biol. 90 (2023) 1–14, https://doi.org/10.1016/j.semcancer.2023.01.007.

[15] M. Quanz, E. Bender, C. Kopitz, S. Grünewald, A. Schlicker, W. Schwede, A. Eheim, L. Toschi, R. Neuhaus, C. Richter, J. Toedling, C. Merz, R. Lesche, A. Kamburov, H. Siebeneicher, M. Bauser, A. Hägebarth, Preclinical efficacy of the novel monocarboxylate transporter 1 inhibitor BAY-8002 and associated markers of resistance, Mol. Cancer Ther. 17 (2018) 2285–2296, https://doi.org/10.1158/1535-7163.MCT-17-1253.

[16] C. Vander Linden, C. Corbet, Killing two birds with one stone: blocking the mitochondrial pyruvate carrier to inhibit lactate uptake by cancer cells and radiosensitize tumors, Mol. Cell. Oncol. 5 (2018) 7, https://doi.org/10.1080/23723556.2018.1465016.

[17] S. Halford, G.J. Veal, S.R. Wedge, G.S. Payne, C.M. Bacon, P. Sloan, I. Dragoni, K. Heinzmann, S. Potter, B.M. Salisbury, M. Chenard-Poirier, A. Greystoke, E. C. Howell, W.A. Innes, K. Morris, C. Plummer, M. Rata, G. Petrides, H.C. Keun, U. Banerji, R. Plummer, A phase I dose-escalation study of AZD3965, an oral monocarboxylate transporter 1 inhibitor, in patients with advanced cancer, Clin. Cancer Res. 29 (2023) 1429–1439, https://doi.org/10.1158/1078-0432.CCR-22-2263.

[18] W. Blaszczak, H. Williams, P. Swietach, Autoregulation of H+/lactate efflux prevents monocarboxylate transport (MCT) inhibitors from reducing glycolytic

lactic acid production, Br. J. Cancer 127 (7) (2022) 1365–1377, https://doi.org/10.1038/s41416-022-01910-7.
[19] V.F. Van Hée, D. Labar, G. Dehon, D. Grasso, V. Grégoire, G.G. Muccioli, R. Frédérick, P. Sonveaux, Radiosynthesis and Validation of (±)-[18 F]-3-fluoro-2-hydroxypropionate ([18 F]-FLac) as a PET Tracer of Lactate to Monitor MCT1-dependent Lactate Uptake in Tumors, 2017, https://doi.org/10.18632/oncotarget.14705.
[20] M. Sadeghzadeh, B. Wenzel, F.-A. Ludwig, K. Kopka, R. Moldovan, P. Brust, Synthesis and radiofluorination of [18F]F-BAY-8002: a novel potential radiotracer for PET imaging of monocarboxylate transporter 1, Nucl. Med. Biol. 96–97 (2021) S74–S75, https://doi.org/10.1016/S0969-8051(21)00386-3.
[21] C. Borsari, D.J. Trader, A. Tait, M.P. Costi, Designing chimeric molecules for drug discovery by leveraging chemical biology, J. Med. Chem. 63 (2020) 1908–1928, https://doi.org/10.1021/acs.jmedchem.9b01456.
[22] C.F. Ramogida, C. Orvig, Tumour targeting with radiometals for diagnosis and therapy, Chem. Commun. 49 (2013) 4720–4739, https://doi.org/10.1039/C3CC41554F.
[23] C. Rodríguez-Rodríguez, M. Telpoukhovskaia, C. Orvig, The art of building multifunctional metal-binding agents from basic molecular scaffolds for the potential application in neurodegenerative diseases, Coord. Chem. Rev. 256 (2012) 2308–2332, https://doi.org/10.1016/J.CCR.2012.03.008.
[24] P. Kręcisz, K. Stefańska, J. Studziński, M. Pitucha, A. Czylkowska, P. Szymański, Radiocopper in radiopharmacy and medical use: current status and perspective, J. Med. Chem. 68 (2025) 2356–2376, https://doi.org/10.1021/acs.jmedchem.4c02885.
[25] U. Søndergaard, K.E. Thomas, K. Søborg Pedersen, M. Kranz, R. Sundset, A. Moldes-Anaya, M. Jensen, Production of 67Cu at a biomedical cyclotron via 70Zn(p,α) 67Cu reaction and its evaluation in a preclinical study using small animal SPECT/CT, Appl. Radiat. Isot. 215 (2025) 111551, https://doi.org/10.1016/J.APRADISO.2024.111551.
[26] D. Rodrigues, A.I. Fonseca, S. do Carmo, J. Sereno, I. Hrynchak, J.N. Moreira, C. Gomes, A. Abrunhosa, Is Copper-61 the new Gallium-68? Automation and preclinical proof-of-concept of 61Cu-based radiopharmaceuticals for prostate cancer imaging, Pharmaceuticals 18 (2025), https://doi.org/10.3390/ph18040469.
[27] C.J. Anderson, R. Ferdani, Copper-64 radiopharmaceuticals for PET imaging of cancer: advances in preclinical and clinical research, Cancer Biother. Radiopharm. 24 (2024) 379–393, https://doi.org/10.1089/cbr.2009.0674.
[28] V. Maheshwari, J.L.J. Dearling, S.T. Treves, A.B. Packard, Measurement of the rate of copper(II) exchange for 64Cu complexes of bifunctional chelators, Inorgan. Chim. Acta 393 (2012) 318–323, https://doi.org/10.1016/J.ICA.2012.07.012.
[29] S. Chaves, R. Delgado, J.J.R.F. Da Silva, The stability of the metal complexes of cyclic tetra-aza tetra-acetic acids, Talanta 39 (1992) 249–254, https://doi.org/10.1016/0039-9140(92)80028-C.
[30] F.K. Kálmán, Z. Baranyai, I. Tóth, I. Bányai, R. Király, E. Brücher, S. Aime, X. Sun, A.D. Sherry, Z. Kovács, Synthesis, potentiometric, kinetic, and NMR studies of 1,4,7,10- tetraazacyclododecane-1,7-bis(acetic acid)-4,10-bis (methylenephosphonic acid) (DO2A2P) and its complexes with ca(II), cu(II), Zn(II) and lanthanide(III) ions, Inorg. Chem. 47 (2008) 3851–3862, https://doi.org/10.1021/ic7024704.
[31] A. Takács, R. Napolitano, M. Purgel, A.C. Bényei, L. Zékány, E. Brücher, I. Tóth, Z. Baranyai, S. Aime, Solution structures, stabilities, kinetics, and dynamics of DO3A and DO3A-sulphonamide complexes, Inorg. Chem. 53 (2014) 2858–2872, https://doi.org/10.1021/ic4025958.
[32] M. Tosato, M. Dalla Tiezza, N.V. May, A.A. Isse, S. Nardella, L. Orian, M. Verona, C. Vaccarin, A. Alker, H. MäcKe, P. Pastore, V. Di Marco, Copper coordination chemistry of sulfur pendant cyclen derivatives: an attempt to hinder the reductive-induced demetalation in 64/67Cu radiopharmaceuticals, Inorg. Chem. 60 (2021) 11530–11547, https://doi.org/10.1021/acs.inorgchem.1c01550.
[33] V. Kubíček, Z. Böhmová, R. Ševčíková, J. Vaněk, P. Lubal, Z. Poláková, R. Michalicová, J. Kotek, P. Hermann, NOTA complexes with copper(II) and divalent metal ions: kinetic and thermodynamic studies, Inorg. Chem. 57 (2018) 3061–3072, https://doi.org/10.1021/acs.inorgchem.7b02929.
[34] A.F. Prasanphanich, L. Retzloff, S.R. Lane, P.K. Nanda, G.L. Sieckman, T.L. Rold, L. Ma, S.D. Figueroa, S.V. Sublett, T.J. Hoffman, C.J. Smith, In vitro and in vivo analysis of [64Cu-NO2A-8-Aoc-BBN(7-14)NH2]: a site-directed radiopharmaceutical for positron-emission tomography imaging of T-47D human breast cancer tumors, Nucl. Med. Biol. 36 (2009) 171–181, https://doi.org/10.1016/j.nucmedbio.2008.11.005.
[35] H. Liu, X. Zhang, J. Zhang, Y. Pan, H. Wen, X. Xu, S. Wu, Y. Wang, C. Zhang, G. Ma, Y. Liu, R. Wang, J. Zhang, Comparison of 64Cu-DOTA-PSMA-3Q and 64Cu-NOTA-PSMA-3Q utilizing NOTA and DOTA as bifunctional chelators in prostate cancer: preclinical assessment and preliminary clinical PET/CT imaging, Eur. J. Nucl. Med. Mol. Imaging 52 (2025) 2792–2803, https://doi.org/10.1007/s00259-025-07131-3.
[36] A. Guillou, L.M.P. Lima, M. Roger, D. Esteban-Gómez, R. Delgado, C. Platas-Iglesias, V. Patinec, R. Tripier, 1,4,7-Triazacyclononane-based bifunctional picolinate ligands for efficient copper complexation, Eur J Inorg Chem 2017 (2017) 2435–2443, https://doi.org/10.1002/ejic.201700176.
[37] R. Chinchilla, C. Nájera, The Sonogashira reaction: a booming methodology in synthetic organic chemistry, Chem. Rev. 107 (2007) 874–922, https://doi.org/10.1021/cr050992x.
[38] S. Puri, K. Stefan, S.L. Khan, J. Pahnke, S.M. Stefan, K. Juvale, Indole derivatives as new structural class of potent and antiproliferative inhibitors of monocarboxylate transporter 1 (MCT1; SLC16A1), J. Med. Chem. 66 (2023) 657–676, https://doi.org/10.1021/acs.jmedchem.2c01612.
[39] K.A. Rubinson, Practical corrections for p(H,D) measurements in mixed H2O/D2O biological buffers, Anal. Methods 9 (2017) 2744–2750, https://doi.org/10.1039/c7ay00669a.
[40] P. Gans, A. Sabatini, A. Vacca, Investigation of equilibria in solution. Determination of equilibrium constants with the HYPERQUAD suite of programs, Talanta 43 (1996) 1739–1753, https://doi.org/10.1016/0039-9140(96)01958-3.
[41] L. Alderighi, P. Gans, A. Ienco, D. Peters, A. Sabatini, A. Vacca, Hyperquad simulation and speciation (HySS): a utility program for the investigation of equilibria involving soluble and partially soluble species, Coord. Chem. Rev. 184 (1999) 311–318, https://doi.org/10.1016/S0010-8545(98)00260-4.
[42] M. Tosato, S. Franchi, A.A. Isse, A. Del Vecchio, G. Zanoni, A. Alker, M. Asti, T. Gyr, V. Di Marco, H. Mäcke, Is smaller better? Cu2+/Cu+ coordination chemistry and copper-64 radiochemical investigation of a 1,4,7-triazacyclononane-based sulfur-rich chelator, Inorg. Chem. 62 (2023) 20621–20633, https://doi.org/10.1021/acs.inorgchem.3c00621.
[43] K.J. Powell, P.L. Brown, R.H. Byrne, T. Gajda, G. Hefter, S. Sjöberg, H. Wanner, Chemical speciation of environmentally significant metals with inorganic ligands part 2: the Cu 2+-OH-, Cl-, CO 3 2-, SO 4 2-, and PO 4 3-systems (IUPAC technical report), Pure Appl. Chem. 79 (2007) 895–950, https://doi.org/10.1351/pac200779050895.
[44] S. Puri, K. Juvale, Monocarboxylate transporter 1 and 4 inhibitors as potential therapeutics for treating solid tumours: a review with structure-activity relationship insights, Eur. J. Med. Chem. 199 (2020) 112393, https://doi.org/10.1016/J.EJMECH.2020.112393.
[45] A. Marlin, I. Hierlmeier, A. Guillou, M. Bartholomä, R. Tripier, V. Patinec, Bioconjugated chelates based on (methylpyridinyl)tacn: synthesis, 64Cu labeling and in vitro evaluation for prostate cancer targeting, Metallomics 14 (2022) 36, https://doi.org/10.1093/mtomcs/mfac036.
[46] E.W. Price, C. Orvig, Matching chelators to radiometals for radiopharmaceuticals, Chem. Soc. Rev. 43 (2013) 260–290, https://doi.org/10.1039/C3CS60304K.
[47] A.A. D'souza, R. Shegokar, Polyethylene glycol (PEG): a versatile polymer for pharmaceutical applications, Expert Opin. Drug Deliv. 13 (2016) 1257–1275, https://doi.org/10.1080/17425247.2016.1182485.
[48] Z. Varasteh, U. Rosenström, I. Velikyan, B. Mitran, M. Altai, H. Honarvar, M. Rosestedt, G. Lindeberg, J. Sörensen, M. Larhed, V. Tolmachev, A. Orlova, The effect of mini-PEG-based spacer length on binding and pharmacokinetic properties of a 68Ga-labeled NOTA-conjugated antagonistic analog of bombesin, Molecules 19 (2014) 10455–10472, https://doi.org/10.3390/MOLECULES190710455.
[49] Q. Wan, H. Yuan, P. Cai, Y. Liu, T. Yan, L. Wang, Z. Zhou, W. Zhang, N. Liu, Effects of PEGylation on imaging contrast of 68Ga-labeled bicyclic peptide PET probes targeting nectin 4, Mol. Pharm. 21 (2024) 4430–4440, https://doi.org/10.1021/ACS.MOLPHARMACEUT.4C00366.
[50] P. Kanellopoulos, E. Bezverkhniaia, A. Abouzayed, U. Rosenström, V. Tolmachev, A. Orlova, Two novel [68Ga]ga-Labeled radiotracers based on metabolically stable [Sar11]RM26 antagonistic peptide for diagnostic positron emission tomography imaging of GRPR-positive prostate cancer, ACS Omega 9 (2024) 18608–18616, https://doi.org/10.1021/acsomega.4c01348.
[51] C. Baun, B. Mitran, S.S. Rinne, J.H. Dam, B.B. Olsen, V. Tolmachev, A. Orlova, H. Thisgaard, Preclinical evaluation of the Copper-64 labeled GRPR-antagonist RM26 in comparison with the Cobalt-55 labeled counterpart for PET-imaging of prostate cancer, Molecules 25 (2020) 5993, https://doi.org/10.3390/MOLECULES25245993.
[52] Y. Liu, L. Xia, H. Li, P. Cai, S. Tang, Y. Feng, G. Liu, Y. Chen, N. Liu, W. Zhang, Z. Zhou, Exploring the impact of PEGylation on pharmacokinetics: a size-dependent effect of polyethylene glycol on prostate-specific membrane antigen inhibitors, EJNMMI Res. 14 (2024) 1–13, https://doi.org/10.1186/s13550-024-01071-z.
[53] Z. Xiao, D. Chen, S. Song, R. Van Der Vlag, P.E. Van Der Wouden, R. Van Merkerk, R.H. Cool, A.K.H.H. Hirsch, B.N. Melgert, W.J. Quax, G.J. Poelarends, F.J. Dekker, 7-hydroxycoumarins are affinity-based fluorescent probes for competitive binding studies of macrophage migration inhibitory factor, J. Med. Chem. 63 (2020) 11920–11933, https://doi.org/10.1021/acs.jmedchem.0c01160.
[54] M. Roger, L.M.P. Lima, M. Frindel, C. Platas-Iglesias, J.F. Gestin, R. Delgado, V. Patinec, R. Tripier, Monopicolinate-dipicolyl derivative of triazacyclononane for stable complexation of Cu2+ and 64Cu2+, Inorg. Chem. 52 (2013) 5246–5259, https://doi.org/10.1021/ic400174r.
[55] V. Stavila, M. Allali, L. Canaple, Y. Stortz, C. Franc, P. Maurin, O. Beuf, O. Dufay, J. Samarut, M. Janier, J. Hasserodt, Significant relaxivity gap between a low-spin and a high-spin iron(II) complex of structural similarity: an attractive off–on system for the potential design of responsive MRI probes, New J. Chem. 32 (2008) 428–435, https://doi.org/10.1039/B715254J.
[56] A. Marlin, F. Le Pape, J. Le Goff, N. Hamon, T. Troadec, R. Tripier, C. Berthou, V. Patinec, New triazacycloalkane derivatives as cytotoxic agents for CLL treatment: from proof of concept to the targeting biomolecule, Bioconjug. Chem. 33 (2022) 1377–1392, https://doi.org/10.1021/acs.bioconjchem.2c00227.
[57] A. Bianchi, M. Micheloni, P. Paoletti, Thermodynamic aspects of the polyazacycloalkane complexes with cations and anions, Coord. Chem. Rev. 110 (1991) 17–113, https://doi.org/10.1016/0010-8545(91)80023-7.
[58] Z. Baranyai, Z. Pálinkás, F. Uggeri, E. Brücher, Equilibrium studies on the Gd3+, Cu2+ and Zn 2+ complexes of BOPTA, DTPA and DTPA-BMA ligands: kinetics of metal-exchange reactions of [Gd(BOPTA)]2, Eur. J. Inorg. Chem. 2010 (2010) 1948–1956, https://doi.org/10.1002/ejic.200901261.
[59] R. Delgado, V. Félix, L.M.P. Lima, D.W. Price, Metal Complexes of Cyclen and Cyclam Derivatives Useful for Medical Applications: A Discussion Based on Thermodynamic Stability Constants and Structural Data, 2007, https://doi.org/10.1039/b704360k.

[60] L. Castellino, E. Alladio, S. Bertinetti, G. Lando, C. De Stefano, S. Blasco, E. García-España, S. Gama, S. Berto, D. Milea, PyES – an open-source software for the computation of solution and precipitation equilibria, Chemom. Intel. Lab. Syst. 239 (2023), https://doi.org/10.1016/j.chemolab.2023.104860.

[61] W. Han, Z.D. Wang, C.Z. Xie, Z.Q. Liu, S.P. Yan, D.Z. Liao, Z.H. Jiang, P. Cheng, Crystal structures and spectroscopic properties of copper(II) and zinc(II) complexes with the macrocycle 1,4,7-tris(2-pyridylmethyl)-1,4,7- triazacyclononane, J. Chem. Crystallogr. 34 (2004) 495–500, https://doi.org/10.1023/B:JOCC.0000042016.86927.1b.

[62] A. Marlin, F. Le Pape, T. Troadec, J. Le Goff, R. Tripier, C. Berthou, V. Patinec, Zn2 + triazamacrocyclic chelators with methylpyridine pendant arms for B-cell apoptosis: a structure–activity study, Dalton Trans. 54 (2025) 3939–3951, https://doi.org/10.1039/D4DT02962C.

[63] N. Elgrishi, K.J. Rountree, B.D. McCarthy, E.S. Rountree, T.T. Eisenhart, J. L. Dempsey, A practical beginner's guide to cyclic voltammetry, J. Chem. Educ. 95 (2018) 197–206, https://doi.org/10.1021/acs.jchemed.7b00361.

[64] A. Rodríguez-Rodríguez, Z. Halime, L.M.P. Lima, M. Beyler, D. Deniaud, N. Le Poul, R. Delgado, C. Platas-Iglesias, V. Patinec, R. Tripier, Cyclams with ambidentate methylthiazolyl pendants for stable, inert, and selective Cu(II) coordination, Inorg. Chem. 55 (2016) 619–632, https://doi.org/10.1021/ACS.INORGCHEM.5B01779.